



Impact of Surface Waves on Mixing and Circulation in a Summertime Lead

Ara Lee¹, Jenny Hutchings¹, Chris Horvat², Aikaterini Tavri², and Brodie Pearson¹

¹College of Earth, Ocean, and Atmospheric Sciences, Oregon State University, Corvallis, OR, USA

²Brown University, Providence, RI, USA

Correspondence: Ara Lee (leear@oregonstate.edu)

Abstract.

Surface waves are becoming more prevalent in the Arctic as sea ice cover reduces. Here we use 3D turbulence-resolving simulations to explore how surface waves affect upper ocean dynamics, and hence surface conditions, as they propagate along summertime leads (narrow regions of open ocean between melting sea-ice cover). We separate the ocean dynamics into turbulent motions which dominate vertical kinetic energy, and a mean cross-lead circulation which drives near-surface downwelling within the lead. Without waves, along-lead winds create weak mixing and an asymmetric circulation where a sinking plume within the lead is balanced by upwelling that extends under the ice to the right of the wind vector. The presence of waves enhances both mixing and circulation by localizing, strengthening and deepening the downwelling plume and turbulent vertical velocities, increasing vertical buoyancy fluxes, and creating an upwelling cell to the left of the wind which significantly alters surface conditions beneath the left lead edge. Waves also drive a sharp front and convection within the lead. Physically-based scalings are proposed for the mixing and circulation changes to capture the effects of various system parameters including lead width, which has a leading-order impact on both turbulence and circulation. The wave-driven changes to turbulence and circulation are present even for relatively weak (developing) waves, although the biggest changes are seen for strong (equilibrium) waves.

15 1 Introduction

The ocean surface boundary layer (OSBL) regulates vital exchanges of momentum, heat, and trace gases between the ocean and atmosphere, playing a crucial role in Earth's climate system. The dynamics of the OSBL are driven by various processes including wind-driven shear turbulence, buoyancy-driven convective turbulence, and wave-driven Langmuir turbulence. OSBL turbulence drives vertical mixing and redistributes heat, energy, and tracers throughout the upper ocean (Belcher et al., 2012). Langmuir turbulence arises from the interaction between surface waves and wind, forming coherent structures called Langmuir cells. In the open ocean, Langmuir turbulence increases vertical mixing and deepens the mixed layer by enhancing entrainment of sub-surface waters (Polton and Belcher, 2007; Pearson et al., 2015, 2019). While Langmuir turbulence has been extensively studied in open-ocean conditions, its role in ice-affected regions is only beginning to be understood. Recent work by Tavri et





al. (2025) using a coupled sea ice—wave model suggests that Langmuir turbulence has high potential in the marginal ice zone (MIZ), and its contribution is expected to increase as sea ice retreats and the MIZ expands.

The Arctic Ocean is undergoing rapid transformation as sea ice retreats, with open water areas increasing significantly (Meier et al., 2024). This retreat can be mechanically amplified by the presence of surface waves, particularly in open water areas within the sea ice (Casas-Prat and Wang, 2020). Leads are narrow regions of open ocean between sea-ice cover, and they play an outsized role in OSBL processes, facilitating ocean-atmosphere exchanges and influencing local and regional sea ice melt, despite occupying less than 10% of the ice cover (Morison and McPhee, 2001). Waves within leads, generated locally by wind or propagating as swell, could create Langmuir turbulence and interact with other OSBL dynamics. Langmuir turbulence in the open ocean has been shown to significantly affect vertical fluxes and the redistribution of heat and momentum (Pearson et al., 2015; Li and Fox-Kemper, 2020), and wave-current interactions alter upper-ocean dynamics (Suzuki and Fox-Kemper, 2016; Sullivan and McWilliams, 2019). Understanding the interplay between waves, Langmuir turbulence, and lead dynamics is critical for improving predictions of Arctic sea ice loss and the resulting impacts on regional and global climates.

Previous work has provided insights into upper-ocean dynamics within leads and ice-affected regions, but important questions remain. Skyllingstad et al. (2005) used 3D large-eddy simulations (LES) to examine shallow (upper 4 m) wind-driven mixing within summertime leads. Ramudu et al. (2018) modeled heat entrainment under solid ice with 3D LES, where turbulence was driven by a combination of melt-driven buoyancy fluxes and ice-driven surface stress. Bourgault et al. (2020) used 3D LES to study upper ocean dynamics in wintertime leads, driven by dense water formation within the lead, representing ice formation, and a cross-lead wind stress curl. Alvarez (2022) conducted 2D simulations of evenly-spaced summertime leads with cross-lead winds, showing that calm conditions and freshwater fluxes beneath melting ice promote sinking at lead centers and lateral heat redistribution, forming near-surface temperature maxima. None of the above studies have explored the effects of surface waves on upper-ocean dynamics around a summertime lead, despite the growing prevalence of waves in the Arctic (Stopa et al., 2016).

Our study provides the first exploration of wave-driven mixed-layer dynamics in ice-affected regions. We analyze 3D-turbulence-resolving numerical simulations of a summertime lead with along-lead winds and waves to explore how turbulence, cross-lead circulation, and tracer evolution are augmented by the presence of surface waves. These simulations provide novel insights into Arctic OSBL processes and identify novel mechanisms through which surface waves could impact sea ice melt.

50 2 Method

2.1 LES model description and basic setup

To simulate upper ocean dynamics including wave effects, we use a model based on the wave-averaged Craik-Leibovich equations, which have been extensively applied in prior LES studies (e.g., McWilliams et al., 1997; Pearson et al., 2015; Suzuki and Fox-Kemper, 2016). The evolution equations (Craik and Leibovich, 1976; Leibovich, 1980) for the Eulerian momentum components ($\mathbf{u} = (u, v, w)$) and buoyancy (b) in this system are:





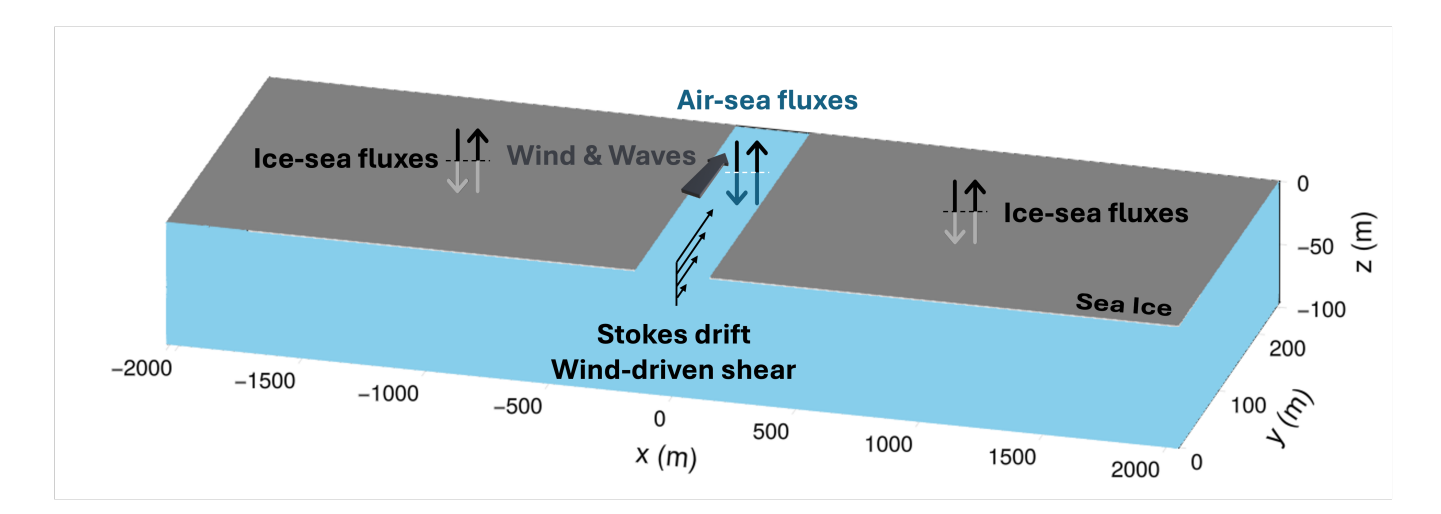


Figure 1. Schematic of LES domains and the physical processes across the lead (drift and flux vectors are not to scale).

$$\nabla \cdot \mathbf{u} = 0, \text{and}$$
 (1)

$$\frac{\partial \mathbf{u}}{\partial t} + (\mathbf{u} \cdot \nabla)\mathbf{u} = -\mathbf{f} \times (\mathbf{u} + \mathbf{u_s}) - \nabla \pi + b\mathbf{g} + \mathbf{u_s} \times \boldsymbol{\omega} - \nabla \cdot \boldsymbol{\tau},$$
(2)

$$\frac{\partial b}{\partial t} + \mathbf{u} \cdot \nabla b = -\mathbf{u}_s \cdot \nabla b - \nabla \cdot \mathbf{q}_b \tag{3}$$

The variables used in the equations are the Stokes drift due to surface waves, $\mathbf{u_s}$, the modified pressure, $\pi = p + \frac{1}{2} |\mathbf{u_s}|^2 + \mathbf{u_s} \cdot \mathbf{u}$ where p is the standard pressure (McWilliams et al., 1997), the Coriolis parameter $f = f\hat{z}$, where \hat{z} is the vertical unit vector, and the relative vorticity $\boldsymbol{\omega} = \nabla \times \mathbf{u}$. The LES subgrid terms are represented through a subgrid momentum flux, $\boldsymbol{\tau} = \tau_{ij}$, and a subgrid buoyancy flux, \mathbf{q}_b . Both are parameterized using the Smagorinsky–Lilly closure (Smagorinsky, 1958), which models the subgrid stresses with an eddy viscosity based on the local strain rate and grid spacing, and the subgrid buoyancy fluxes with an analogous eddy diffusivity formulation. Buoyancy, b, is defined in terms of water density as $b = g(\rho_0 - \rho)/\rho_0$, with ρ and ρ_0 representing the density and reference density, respectively.

The simulations are conducted using *Oceananigans.jl*, an LES model developed in Julia (Ramadhan et al., 2020). This model evolves the Lagrangian momentum, but with an equation set that is formally equivalent to the Eulerian governing equations of Eq. 1 and 2. A schematic of the LES domain and important physical processes are shown in Fig. 1. The standard set up for the simulations in this study uses a computational domain $(L_x, L_y, L_z) = (4096, 256, 96)$ m with uniform grid spacing of $\Delta x = \Delta y = 1.0$ m and $\Delta z = 0.5$ m, a 300 m wide lead centered at x = 0 and extending along the y-axis, periodic horizontal





boundary conditions, and a stress-free bottom boundary conditions. To minimize wave reflection and ensure numerical stability, a damping layer is implemented close to the *x*-boundaries as detailed in Appendix A.

Simulations are initialized with zero Lagrangian momentum ($\mathbf{u_L} = \mathbf{u} + \mathbf{u_s} = 0$), superposed with small random noise. Initial temperature and salinity profiles are based on SHEBA observations from 18 to 26 July 1998 (Stanton and Shaw, 2016). These profiles feature an initial mixed layer depth of approximately 7 m, consistent with those used by Alvarez (2022). Since the water is near-freezing, density is treated using a salinity-dependent linear equation of state, $\rho = \rho_0[1 + \beta(S - S_0)]$, where ρ_0 is the reference density, S_0 is the reference salinity, and β is the haline contraction coefficient, and temperature is modeled as a passive tracer analogous to the approach of Alvarez (2022). Outside of the lead, ice-ocean fluxes affect buoyancy (through salinity) and temperature. The ice-ocean buoyancy fluxes are based on ice melt rates imposed as $\frac{dh_{ice}}{dt} = 0.5$ cm/day, where h_{ice} is the ice thickness. There are no ice-ocean momentum fluxes, equivalent to stationary ice. This is a one-way coupling, where the ice conditions are imposed on the ocean, and the ice properties do not change over time. Details of the ice-ocean boundary conditions and flux formulations are included in Appendix A.

The simulation forcing includes winds blowing along the lead in addition to wind-aligned waves propagating within the lead which decay under the ice at the lead edges. The wind stress in all experiments corresponds to a 10-meter wind speed $V_{10}=5$ m/s aligned with the y-axis, and is only applied within the lead. Following Eq. 2, the effects of waves are imposed through an y-aligned Stokes drift which decays exponentially with depth, $v_s(x,z)=v_{s0}e^{2kz}\chi(x)$, where v_{s0} is the surface Stokes drift, and k is the wavenumber of the surface waves (which are assumed to be monochromatic for simplicity). The relative strength of wind and waves is varied across our simulations, which can be encapsulated by the Langmuir number $La_t, \sqrt{\frac{u_s}{v_{s0}}}$, where u_* is the surface friction velocity. A Langmuir number, $La_t=0.3$, represents typical equilibrium windwave conditions, while larger La_t values represent younger (developing) seas. The amplitude of waves is homogeneous in the lead, but decays under the ice within a 90 m-wide wave-affected region (WAR) adjacent to the lead as described in Appendix B. The base simulation parameters are described above. Table 3 summarizes the full set of sensitivity experiments, listing the

2.2 Analysis framework

parameters varied and their explored ranges.

The system is statistically homogeneous along the lead (y-direction) but varies in the cross-lead and vertical (x-z) directions. To represent these variations, fields at any given moment in time, g, are decomposed into an along-lead mean component, $\langle g \rangle$, where $\langle \cdot \rangle$ denotes an average over the along-lead (x) direction, and a turbulent component ($g'(x,y,z) = g(x,y,z) - \langle g \rangle(x,z)$). The averaging is applied only to the resolved Eulerian velocity fields. Turbulent fluxes and variances are then calculated as $\langle f'g' \rangle = \langle fg \rangle - \langle f \rangle \langle g \rangle$ and $\langle g'g' \rangle = \langle gg \rangle - \langle g \rangle \langle g \rangle$, respectively. Note that $\langle g' \rangle = 0$ and $\langle g'\langle f \rangle \rangle = 0$ by definition. This is analogous to standard Reynolds averaging methods for upper ocean turbulence, except the mean in this case contains both the full horizontal mean, which is a function of depth (z) only, and the cross-lead circulation, which has both cross-lead and depth (x - z) structure.

We define both temporal and spatial averaging operators. The temporal average is taken over one inertial cycle, corresponding to approximately 12.5 hours in our simulations. Temporal averages are computed from the final day of integration, after the





105 simulations have been run for two days. Unless otherwise stated, all analyses in this study are presented as inertial-cycle averages.

To compute vertical profiles of properties, we also apply cross-lead (x) averaging in sub-regions of the x-domain. In particular, the *lead average* is the horizontal average taken across the entire lead,

$$\overline{\langle \cdot \rangle}^{\text{lead}}(z) = \frac{1}{L_{\text{lead}}} \int_{-L_{\text{lead}}/2}^{L_{\text{lead}}/2} (\cdot)(x, z, t) \, dx, \tag{4}$$

where L^{lead} is the prescribed lead width and (\cdot) denotes the variable of interest. This operator indicates the mean cross-lead structure of the flow and serves as the primary horizontal x-averaging operator throughout the analysis.

3 Results

3.1 Mean Currents & Cross-lead Circulation

Figure 2 shows the cross-lead structure of the mean flow $(\langle w \rangle, \langle u \rangle)$ and the cross-lead circulation $(\langle \psi \rangle)$ that develop in and around a lead. Results are shown for a control case without surface waves and for a wave-forced case. Both the control and wave-forced cases are forced with the same wind corresponding to a 10-m wind speed of $U_{10} = 5 \text{ m s}^{-1}$. In the wave-forced case, the Stokes drift is imposed with a surface Stokes drift velocity of $v_{s0} = 0.069 \text{ m s}^{-1}$ and a decay depth of approximately 4.8 m. To interpret the structure of the currents and circulation, and how they changes in the presence of waves, in $\langle w \rangle$, $\langle u \rangle$ and $\langle v \rangle$ as the system changes, it will be useful to consider the budgets for these terms. The budget for the velocity components (Eq. 2) can be rearranged as (Suzuki and Fox-Kemper, 2016),

$$\frac{\partial \mathbf{u}}{\partial t} + \mathbf{u}_{\mathbf{L}} \cdot \nabla \mathbf{u} = -u_{L,j} \nabla u_{s,j} - \mathbf{f} \times \mathbf{u}_{\mathbf{L}} + \mathbf{b} + \mathbf{D}_{\mathbf{u}} - \nabla p, \tag{5}$$

where $\mathbf{u_L} = \mathbf{u} + \mathbf{u_s}$ is the Lagrangian velocity and $\mathbf{D^u}$ represents diffusion. The budget for $\langle w \rangle$ can be derived by taking the along-lead average of the vertical component of this equation,

$$\frac{D_L \langle w \rangle}{Dt} = -v_s \frac{\partial v_s}{\partial z} - \langle v \rangle \frac{\partial v_s}{\partial z} - \nabla \cdot \langle \mathbf{u}' w' \rangle - \frac{\partial \langle p \rangle}{\partial z} + \langle b \rangle + \langle D_w \rangle,$$

$$= -\langle v_L \rangle \frac{\partial v_s}{\partial z} - \nabla \cdot \langle \mathbf{u}' w' \rangle - \frac{\partial \langle p \rangle}{\partial z} + \langle b \rangle + \langle D_w \rangle,$$
(6)

where $\langle v_L \rangle = v_s + \langle v \rangle$ is the mean Lagrangian along-lead current and $\frac{D_L}{Dt} = \frac{\partial}{\partial t} + \langle \mathbf{u_L} \rangle \cdot \nabla$ is the Lagrangian derivative. Similarly, the budgets for the currents $\langle u \rangle$ and $\langle v \rangle$, in the cross-lead and along-lead directions respectively, are,





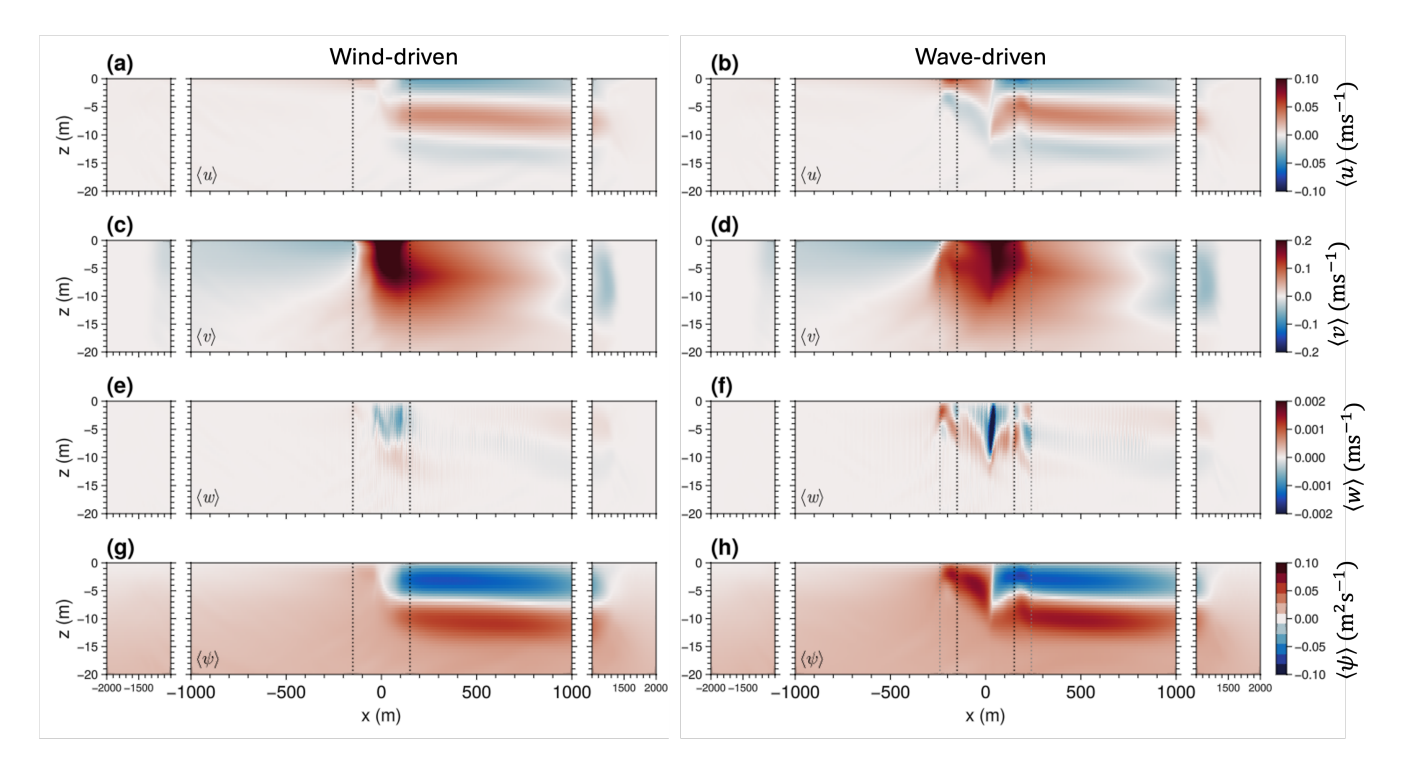


Figure 2. Mean flow and cross-lead circulation of (left) a lead without waves and (right) a lead with waves. Panels show the (a,b) cross-lead velocity $\langle u \rangle$, (c,d) along-lead velocity $\langle v \rangle$, (e,f) vertical velocity $\langle w \rangle$, and (g,h) streamfunction $\langle \psi \rangle$. Fields are spatially averaged in the along-lead direction and temporally averaged over an inertial cycle (\sim 12.5 hr). The central region (x = [-1000, 1000] m) is magnified to better visualize the structures within and around the lead, and the far-field regions (x = [-2000, -1000] m and x = [1000, 2000] m) are displayed separately on compressed x-axes. Black dotted lines indicate the ice lead, and gray dotted lines indicate the wave-affected areas in the wavy experiments.

$$\frac{D_L \langle u \rangle}{Dt} = -\langle v_L \rangle \frac{\partial v_s}{\partial x} + f \langle v_L \rangle - \nabla \cdot \langle \mathbf{u}' u' \rangle - \frac{\partial \langle p \rangle}{\partial x} + \langle D_u \rangle. \tag{7}$$

$$\frac{D_L \langle v \rangle}{Dt} = -f \langle u \rangle - \nabla \cdot \langle \mathbf{u}' v' \rangle + \langle D_v \rangle. \tag{8}$$

30 where we have used the properties that waves are aligned with the lead and $\partial_y \langle \phi \rangle = 0$ for all ϕ .

3.1.1 Wind- and Buoyancy-driven Circulation

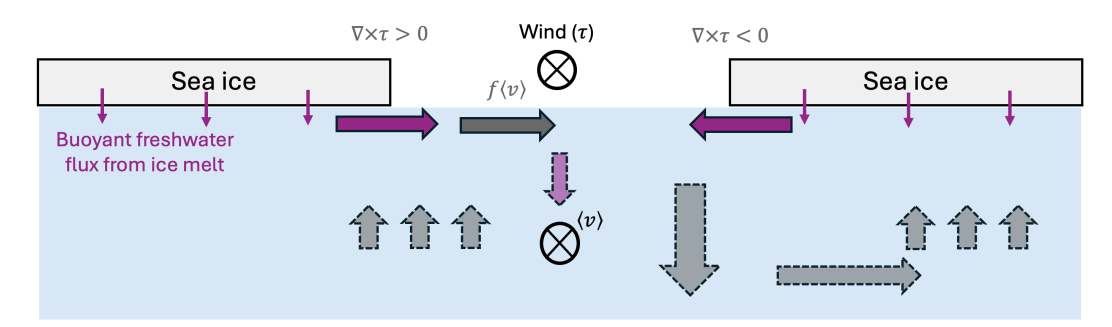
135

In the absence of surface waves, the upper ocean dynamics in and around the lead (Figure 2 left panels) are driven by a combination of wind stress supplying momentum at the surface within the lead and buoyant freshwater fluxes beneath the ice flowing into the lead to displace and push down the denser (saltier) lead surface water. The net result of these wind- and buoyancy-driven forces on cross-lead and vertical velocities are schematized in the top panel of Figure 3. The along-lead





Wind- and ice melt-driven circulation



Wave-driven circulation

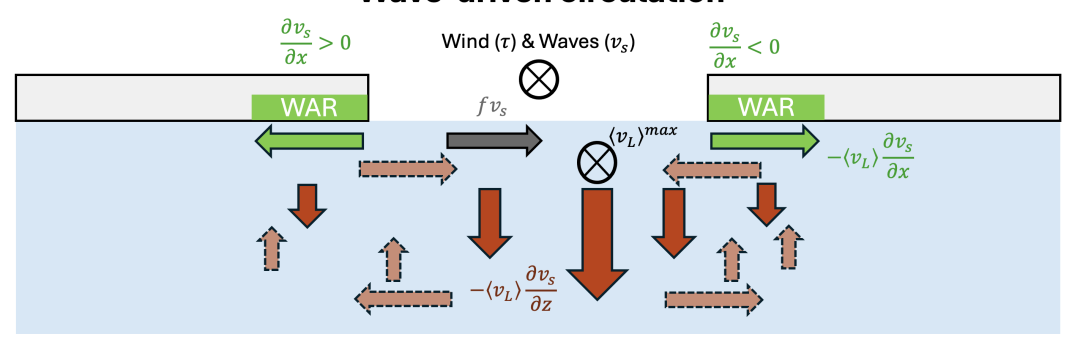


Figure 3. Schematic showing the vertical and cross-lead forces in the near-surface layer resulting from (top) along-front winds and sea-ice melt and (bottom) along-lead waves propagating within the lead and wave-affected region (WAR). In the bottom panel, it is assumed that wind and waves are aligned. Solid arrows show several forces in Eqs. 6 and 7, while dashed arrows show indirect effects of this forcing that result from incompressibility (i.e., forced surface convergence must also produce downwelling).

wind stress provides momentum to the ocean, which results in both along-lead and Coriolis-induced cross-lead flow (Figures 2a,c). The lateral stress gradients at each edge of the lead are opposite in sign, and create opposing wind stress curls. Wind stress curl drives surface convergence and downwelling when $f\nabla \times \tau < 0$, or drives surface divergence and upwelling when $f\nabla \times \tau > 0$. Despite the anti-symmetry of forcing across the lead, the downwelling is intense and localized on the right side of the lead while there is no significant upwelling apparent on the left side of the lead (Fig. 2e). This asymmetry is consistent with the simulations of wind-forced leads in Bourgault et al. (2020), where leads were forced by single-signed wind stress curl in contrast to the alternating wind stress curl across the lead applied in the present simulations. Similar to our simulations, Bourgault et al. (2020) found a strong asymmetric response of upper ocean dynamics to wind forcing where upwelling lead systems were characterized by diffuse and weak upwelling, while downwelling lead systems contained intense and narrow downwelling jets.

The asymmetry of the lead system is also apparent in the cross-lead velocity (Fig. 2a) and the circulation visualized through the streamfunction: $\langle \psi(x,z) \rangle = \int_H^z \langle u \rangle(x,z^*) dz^*$ with the boundary condition $\psi(x,H) = 0$. The water that is downwelled





within the upper 6 m on the right side of the lead circulates 100's of meters horizontally under the ice to the right of the lead before upwelling 300-800m from the lead under the ice, and returning to the lead in a near-surface layer. There is a comparable counter-rotating circulation (blue cell) at depth, which we will not discuss in detail as it occurs below the actively-mixing layer and so does not impact near-surface conditions.

The freshwater flux beneath the ice, but not in the lead, creates a mean pressure gradient $\partial \langle p \rangle / \partial x$ that drives cross-lead flow $\langle u \rangle$ into both side of the lead. This buoyancy-driven circulation is relatively weak in isolation (see Appendix C), but changes in the ice melt rate do have a small, systematic impact on the overall dynamics within lead, which is quantified in Section 3.4.

3.1.2 Wave-driven Circulation

There are two substantial changes to cross-lead circulation when strong waves ($La_t = 0.3$; equivalent to equilibrium windwaves) are added to the system: downwelling becomes more intense, localized, and deeper, and a circulation develops on the left side of the lead (Fig. 2 right column). Both v_s and $\langle v \rangle$ are aligned with lead, which creates a surface-intensified downward force ($-\langle v_L \rangle \partial_z v_s$; Eq. 6) in the lead and adjacent wave-affected regions that is strongest on the right side of the lead (Fig. 2f) where $\langle v_L \rangle = \langle v \rangle + v_s$ reaches its maximum (Fig. 2d). This wave-driven downward force becomes weaker towards the lead edges and under the wave-affected region (WAR) as both the current and waves are reduced. Incompressibility requires that the intense localized downwelling must be accompanied by convergence of cross-lead currents at the surface, divergence of cross-lead currents at depth, and associated upwelling near the edges of the lead and WAR (brown dashed arrows in Fig. 3). This produces a new wave-driven circulation on the left of the lead that extends to the edge of the WAR and impacts near-surface conditions experienced by the ice edge (see Section 3.3.1). The waves also intensify the circulation on the right side of the lead and alter its shape due to upwelling at the right side of the lead and WAR (Fig. 2b vs. Fig. 2a). The lateral wave forces $(-\langle v_L \rangle \partial_y v_s)$ are confined to the WAR and drive divergence of water in the lead. These lateral forces do not significantly impact the circulation of this system, even when the WAR width (i.e., $\partial_v v_s$) is changed (see Appendix B).

3.2 Turbulence & Mixing

The variance of the turbulent vertical velocity ($\langle w'w' \rangle$; or twice the vertical turbulence kinetic energy [TKE]) is an important variable that characterizes the intensity of turbulence and its associated vertical mixing. The budget for $\langle w'w' \rangle$ can be derived from Eq. 5 (Harcourt, 2013),

$$\frac{D_L \langle w'w' \rangle}{Dt} = -2 \langle v'w' \rangle \frac{\partial v_s}{\partial z} + 2 \langle w'b' \rangle - 2 \langle u'w' \rangle \frac{\partial \langle w \rangle}{\partial x} - 2 \langle w'w' \rangle \frac{\partial \langle w \rangle}{\partial z} + \Pi_{ww} - T_{ww} - 2\varepsilon_{ww}, \tag{9}$$

where the terms from left to right represent sources or sinks of vertical TKE due to waves, vertical buoyancy fluxes, lateral shear, pressure terms (Π_{ww}) (Pearson et al., 2019), turbulent transport (T_{ww}), and dissipation (ε_{ww}).

Figure 4a shows a snapshot of the near-surface vertical velocity field ($w = \langle w \rangle + w'$) at z = -2 m and t = 48 hr in the wind-driven (ST) case. The vertical velocity is dominated by spatially intermittent turbulence that is strongest on the right side of the lead, coincident with the broad circulation downwelling region shown in Figure 2b ($x = -50 \rightarrow 150$ m) and the rightward





185

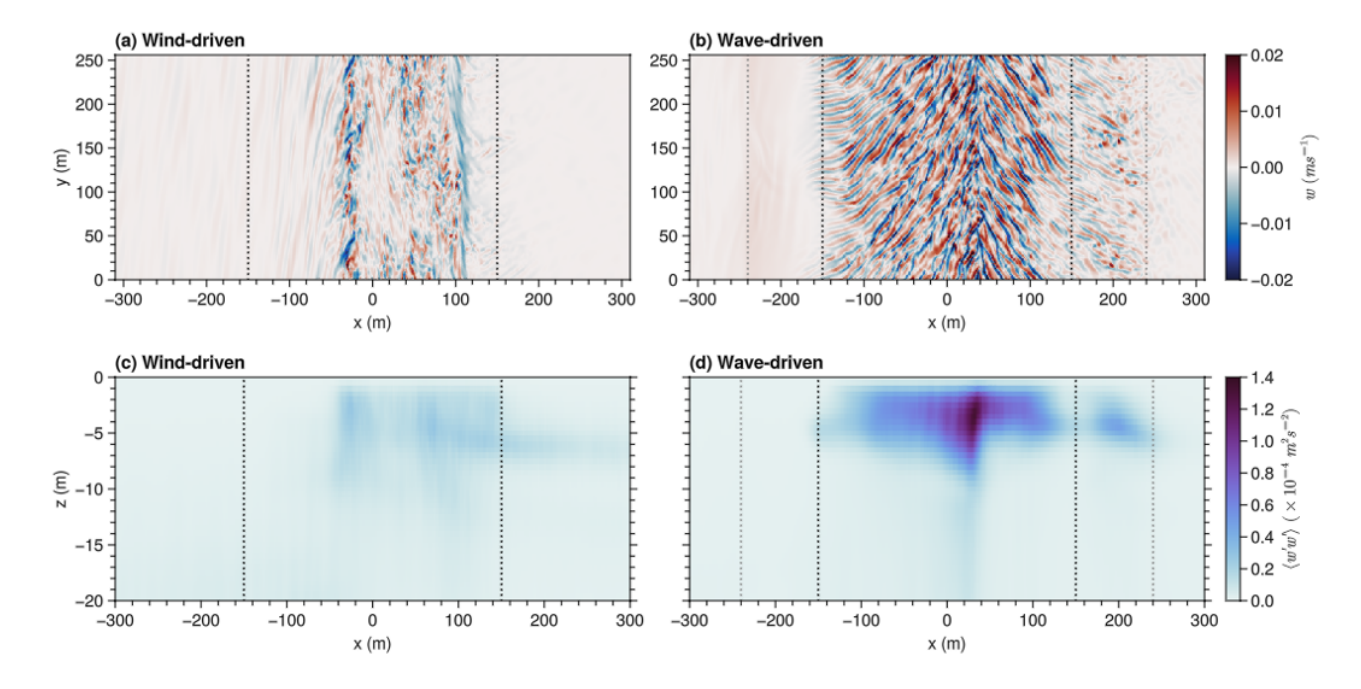


Figure 4. Comparison of turbulence within lead for (left) wind-driven and (right) wave-driven conditions. (a, b) Snapshots of vertical velocities (w) at z=-2 m at t=48 hr in the x-y plane. Also shown are cross-sections of along-lead (y) averaged turbulent (c, d) vertical velocity variance $(\langle w'w'\rangle)$ and (e, f) vertical buoyancy flux $(\langle w'b'\rangle)$ across the lead. Black dotted lines denote the boundaries of the ice lead, while gray dotted lines mark the wave-influenced regions.

advection expected from the Ekman transport forced by surface stress in the lead. Across all depths, the vertical kinetic energy is dominated by turbulence rather than circulation ($\langle w'w' \rangle \gg \langle w \rangle \langle w \rangle$; not shown), and this turbulent $\langle w'w' \rangle$ is concentrated on the right side of the lead (-25 m < x < 100 m) and over the upper 5m of the water column.

The presence of waves generates alternating downwelling and upwelling streaks near the surface, consistent with classical Langmuir cells (Figure 4b). These cells are weak at the lead edges, where sub-ice water flows into the lead, but strengthen and align with the wind and wave vector as they move further into the lead, converging at approximately $x \approx 40m$. This behavior is similar to Langmuir cells observed in frontal convergence zones (Hamlington et al., 2014). Waves energize turbulent kinetic energy within the upper ocean across the entire lead (Fig. 4d vs. 4c) due to the Stokes production (Eq. 9; $-2\langle v'w'\rangle \frac{\partial v_s}{\partial z}$). The most intense $\langle w'w'\rangle$ occurs at the downwelling jet (Fig. 2f). This co-location of turbulence and circulation extrema could impact mixing and entrainment effects of upper ocean turbulence (e.g., Section 3.3.1).

3.3 Effects of Varying Wave Strength

Strong wave activity enhances the depth-averaged $\langle w'w' \rangle$ across the entire lead Fig. 5a, with the most intense $\langle w'w' \rangle$ where the circulation is predominantly downwelling (Figures 2f & 5a). For weak or developing waves there is still a localized maximum





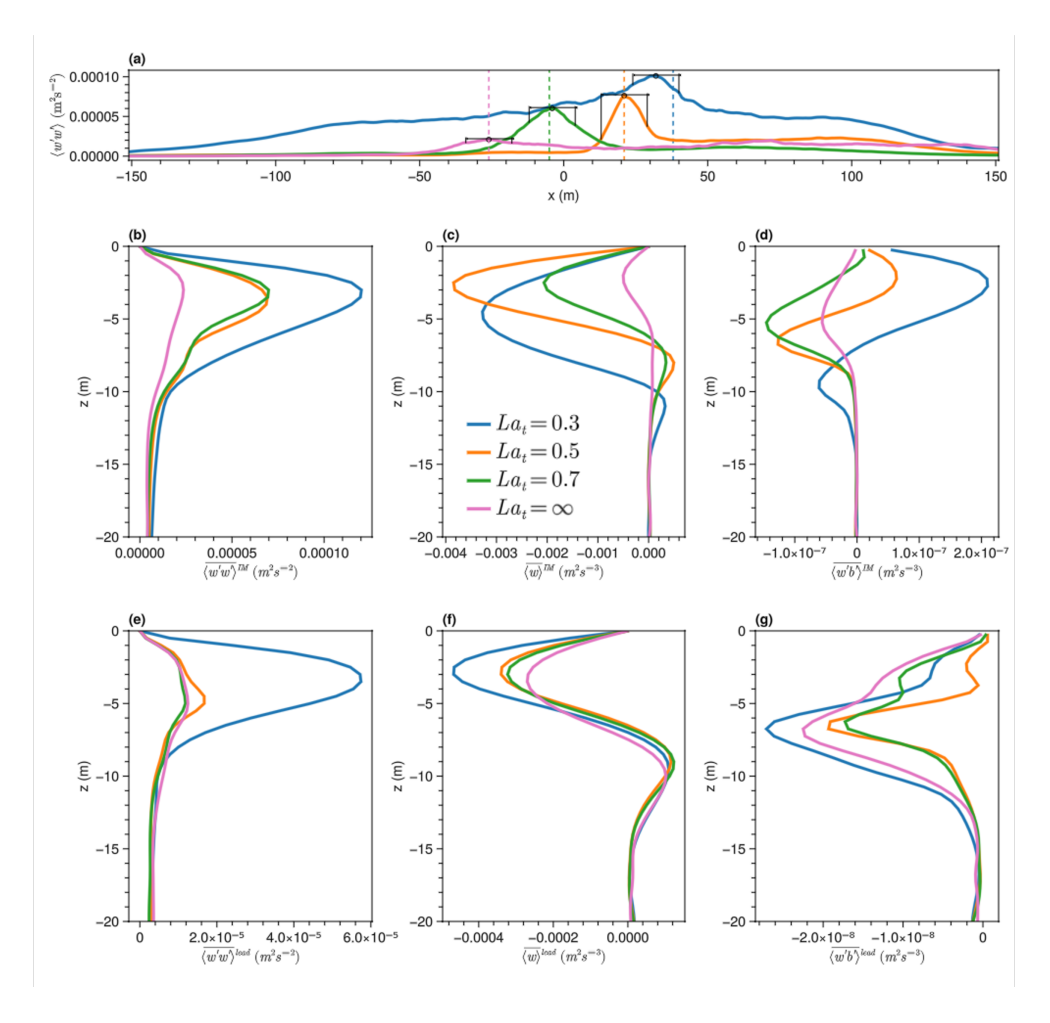


Figure 5. Turbulence and circulation profiles as a function of wave strength. (a) Cross-lead profiles of $\langle w'w' \rangle$ averaged over the top 10 m of the ocean, where dashed vertical lines represent the peak of $\langle w \rangle \langle w \rangle$. Lower panels show vertical profiles of (left) $\langle w'w' \rangle$, (center) $\langle w \rangle$ and (right) $\langle w'b' \rangle$ averaged over the (middle row) intense mixing [IM] region and (bottom row) over the entire lead. All variables are also time-averaged over one inertial cycle. Profiles are shown for various Langmuir numbers ($La_t = 0.3, 0.5, 0.7, \text{and} \infty$)

in vertical TKE coincident with the downwelling circulation region (Figure 5a-b), but the lead-averaged vertical TKE is less elevated (Figure 5d-e). Surface waves influence where $\langle w'w' \rangle$ is most intense within the lead (Figure 5a). The location of most intense $\langle w'w' \rangle$ shifts to the right of the lead as wave forcing becomes stronger (La_t decreases). Strong waves ($La_t = 0.3$) substantially increase $\langle w'w' \rangle$ across the entire lead, resulting in a lead-averaged $\langle w'w' \rangle$ that is approximately 5 times larger than the simulations with weaker waves or no waves (Figure 5e). This energized upper ocean turbulence under wave-forced conditions is consistent with the dominance of a Langmuir turbulence regime (Grant and Belcher, 2009) and associated Stokes production of $\langle w'w' \rangle$ (Eq. 9; $\propto -\langle v'w' \rangle \frac{\partial v_s}{\partial z}$).



205

220

225



To distinguish the behavior of dynamics close to the downwelling region from the dynamics across the entire lead, we compute profiles of $\langle w'w' \rangle$, $\langle w \rangle$ and $\langle w'b' \rangle$ by computing both a y-average over the entire lead $\left(\overline{\langle \cdot \rangle}^{lead} \right)$ and a y-average over the 20m-wide "intense mixing" [IM] region centered on the $\langle w'w' \rangle$ peak $\left(\overline{\langle \cdot \rangle}^{IM} \right)$.

The *intense-mixing average* is designed to isolate the region of strongest turbulent activity. We first compute cross-lead profiles of the vertical velocity variance, $\langle w'w' \rangle$, averaged over the upper $10\,\mathrm{m}$ of the ocean (Figure 5a). The horizontal location of the maximum value of this profile is identified, and an averaging window of $\pm 10\,\mathrm{m}$ around this peak is then used to define the averaging domain,

$$\overline{\langle \cdot \rangle}^{\text{IM}}(z) = \frac{1}{20 \,\text{m}} \int_{x_{\text{peak}} - 10 \,\text{m}}^{x_{\text{peak}} + 10 \,\text{m}} (\cdot)(x, z, t) \, dx, \tag{10}$$

where x_{peak} is the cross-lead position of maximum $\langle w'w' \rangle$ (averaged in the top 10 m). This operator provides a focused measure of the core mixing region and is employed only when examining diagnostics that require localization of turbulent intensity.

These profiles are shown in Figure 5b-g. The presence of waves, whether weak or strong, produces a localized region of more intense $\langle w'w' \rangle$ (Fig. 5b) and downwelling (Fig. 5c) in the intense mixing region near the center of the lead. However, $\langle w'w' \rangle$ and $\langle w \rangle$ averaged across the lead are only elevated for the strongest waves (Fig. 5e & f). The localization (or horizontal heterogeneity) of intense mixing and circulation has the potential to significantly influence surface and ice-ocean conditions by locally entraining deep water and transporting it to the surface and other locations, which will be discussed further in Section 3.3.1.

3.3.1 Impact on Near-surface & Ice-ocean Interface Conditions

Since the presence of surface waves influences circulation and turbulence within the lead system, here we investigate how waves affect near-surface conditions within and around the lead. This will be explored in the context of cross-lead variations in near-surface salinity (equivalent to buoyancy since temperature is a passive tracer). Figure 6 shows the spatial distribution of near-surface salinity change, $\langle S - S_i \rangle$ where S_i is the initial salinity at t=0, at a depth of z=-1.0 m which corresponds to the second grid cell below the surface for varying wave strength. Near-surface salinity generally decreases under the ice to both the left of the wind and far from the lead to the right of the wind, due to the freshwater fluxes imposed to represent ice melt. To the right of the most intense downwelling region of each system, the near-surface salinity is not affected by the presence of waves, as the cross-lead circulation still replenishes the surface with saltier water that originates in the lead or at depth in all experiments (Fig. 6b-e).

The near-surface salinity on the left-side of the lead increases and is significantly affected by the wave forcing, where stronger waves lead to a larger increase of salinity that extends from the intense downwelling region, across the left side of the lead, and, in the wavey simulations, into the wave-affected region [WAR] beneath the ice. Since there are no surface salinity sources (only sinks via ice melt), these surface salinity increases are caused by salty sub-surface water mixing with, or displacing, the





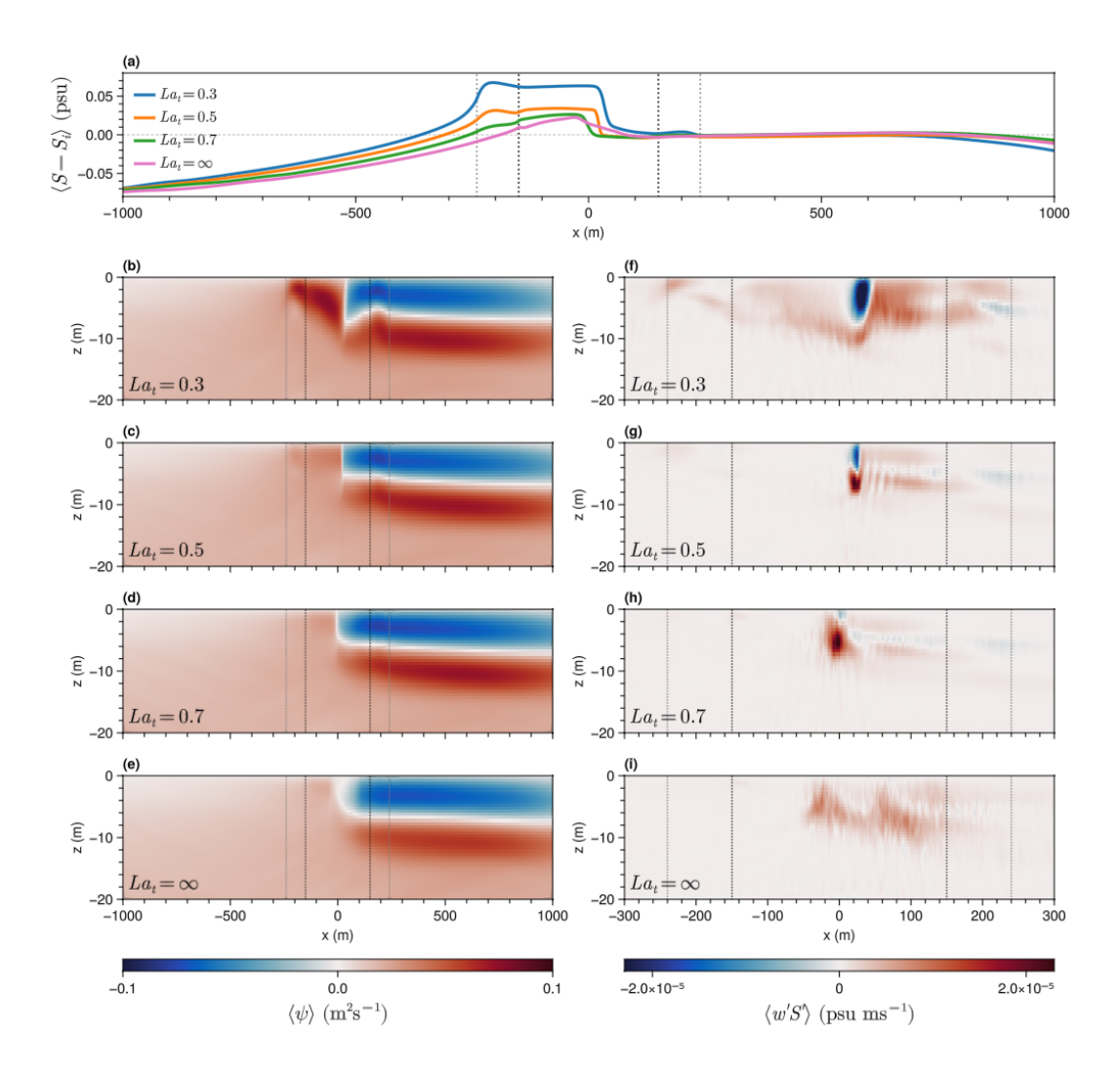


Figure 6. (a) Spatial distribution of salinity differences at a depth of z=-1 m. (Left column) Streamfunction of cross-lead circulation for different Langmuir numbers: (b) La_t = 0.3, (c) La = 0.5, (d) La_t = 0.7, and (e) La = ∞ . Positive values indicate clockwise circulation, while negative values indicate counterclockwise circulation. (Right column) Turbulent salinity flux for different Langmuir numbers: (f) La_t = 0.3, (g) La = 0.5, (h) La_t = 0.7, and (i) La = ∞ .

surface water. It follows that these salinity increases are caused by the wave-driven circulation on the left side of the lead that strengthens with increasing wave forcing (Fig. 6 left panels). This circulation downwells near the lead center and then circulates water back up to the surface under the WAR, to be drawn back into the lead along the surface. If this were purely a circulating system, there would be no change in surface salinity since the water downwelled from the surface would be circulated back to the surface with the same properties. However, the presence of turbulence provides irreversible mixing, particularly near the mixed layer base where entrainment can occur.



245

250

260

265



The changes in turbulent entrainment are highlighted by the turbulent salinity flux $\langle w'S' \rangle$ cross-sections (Fig. 6 right panels) and $\langle w'b' \rangle$ profiles (Fig. 5 right panels) - note that the two fluxes are opposite in sign as $\langle w'b' \rangle = -\beta g \langle w'S' \rangle$. The addition of waves, even weak ones, creates a localized region of intense buoyancy fluxes near the center of the lead that enhance and deepen the entrainment in this intense mixing region (Fig. 5d) which is not as apparent when looking at the lead as a whole (Fig. 5g). Based on the asymmetry of surface salinity changes across the lead, this wave-driven entrainment of deeper saltier water is primarily drawn into the new circulation on the left of the lead, ultimately increasing surface salinity when the water is upwelled in the left WAR. There is a second interesting feature of the intense $\langle w'b' \rangle$ region near the lead center. As waves increase in strength, a positive buoyancy flux (Fig. 5d) or negative salinity flux (blue on Fig. 6f,g) develops near the surface in the intense mixing region. This is indicative of convective turbulence in the upper ocean, despite the experiments having no destabilizing surface buoyancy fluxes, which is the typical driving mechanism of upper ocean convection. This convection is facilitated by the sharp salinity front that develops within the lead with waves (Fig. 6a), as any salty surface water advected into the lead from the left that overshoots the salinity front will induce convective instability. This additional localized convective mixing is not apparent in the lead averaged profiles (Fig. 5g) but provides a positive feedback mechanism for additional localized turbulence near the lead center in the presence of waves, enhancing the depth and strength of mixing, downwelling and entrainment in the intense mixing region.

On the right side of the lead there is little change in the surface salinity when waves are added to the system, consistent with the presence of clockwise circulation on the right of the lead in all experiments (Fig. 6 left panels). This results in the formation of pronounced salinity fronts near the surface at the circulation edges. Beyond the left edge of the lead of WAR (in wavey simulations), weak circulation and the absence of significant turbulence result in minimal salinity changes.

255 3.4 Sensitivity of Ocean Dynamics to Ice-ocean & Wave Properties

The response of ocean dynamics across the lead to variations in environmental and physical parameters provides insights into how leads and waves shape upper-ocean dynamics, and enables the development of scalings and parameterizations for the dominant physical processes. In the following section, we analyze sensitivity tests to evaluate the how changes in melt rate (or freshwater flux), wave properties, lead width, and mixed layer depth affect profiles of $\langle w'w' \rangle$, $\langle w \rangle$ and $\langle w'b' \rangle$ averaged across the lead. We focus this exploration to strongly wave-affected conditions, leaving exploration of the expansive parameter space of wind-driven and mixed regimes to future work. In Section 4 this analysis will be used to build scalings for the dynamics of the lead system.

Longer surface waves lead to decreased turbulent vertical velocity variance $\overline{\langle w'w'\rangle}^{lead}$ and slightly decreased turbulent entrainment $\overline{\langle w'b'\rangle}^{lead}$, but do not affect the circulation within the lead $\overline{\langle w\rangle}^{lead}$ (Figure 7). To explain the behavior of $\overline{\langle w'w'\rangle}^{lead}$ in response to surface wave length changes, it makes sense to start at it's budget (Eq. 9). Ignoring the high-order or diffusive terms, and assuming that the wave and buoyancy terms dominate this system, it would seem reasonable to propose a model of the form,

$$\frac{\langle w'w'\rangle}{\tau} \propto -\langle v'w'\rangle \frac{\partial v_s}{\partial z} + \langle w'b'\rangle \tag{11}$$



280



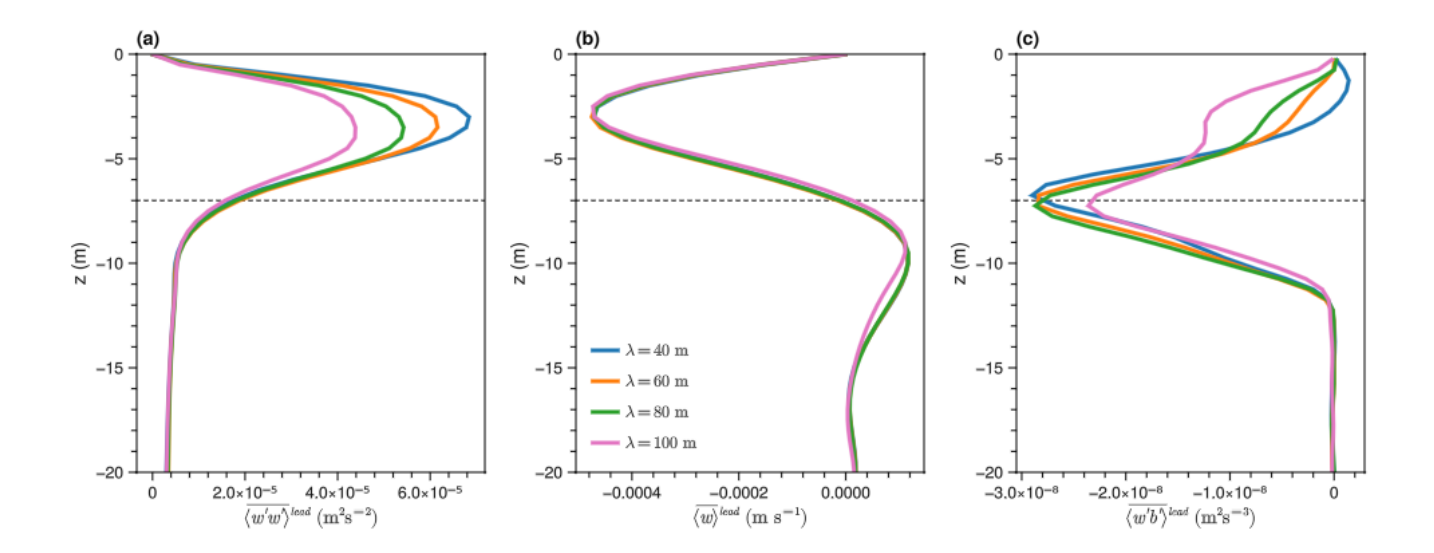


Figure 7. Sensitivity of turbulence and circulation to surface wave length $\lambda = 4\pi\delta$. Lead-averaged profiles of (a) turbulent vertical velocity variance $\overline{\langle w'w' \rangle}^{lead}$ (b) circulation downwelling $\overline{\langle w \rangle}^{lead}$, and (c) turbulent vertical buoyancy flux $\overline{\langle w'b' \rangle}^{lead}$. The dashed line denotes the initial mixed layer depth, h_{init} . Profiles are temporally averaged over one inertial cycle.

where τ represents a timescale over which turbulence kinetic energy is dissipated or decays. Importantly, the Stokes production term depends on the product of the Stokes drift vertical shear and the along-wave momentum flux, which both decrease with depth (Grant and Belcher, 2009). As waves get longer, more of their gradient occurs deeper in the mixed layer, or below the mixed layer, where the momentum flux is smaller than its near-surface value. This mechanism could explain the reduced $\overline{\langle w'w' \rangle}^{lead}$ for longer wavelengths seen in Figure 7.

As the sub-ice freshwater flux (or ice melt rate) increases, there is a decrease in $\overline{\langle w'w'\rangle}^{lead}$ and a slight increase in mixed layer depth, peak circulation downwelling (near-surface minimum $\overline{\langle w\rangle}^{lead}$, herein $\overline{\langle w\rangle}^{lead}_{min}$), and entrainment $(\overline{\langle w'b'\rangle}^{lead})$ minimum), as shown in Figure 8. While ice melt does not directly stabilize the surface in the ice-free lead portion of the domain, freshwater fluxes outside the lead flow into the lead (Appendix C) resulting in a buoyant near-surface layer within the lead. Mixing near-surface buoyant water within the lead over the depth of the mixed layer requires work which would manifest as a negative buoyancy term in Eq. 11 that becomes more negative as the sub-ice freshwater flux increases. Consistent with Figure 8a, faster ice melt rates should result in a greater sink of the $\overline{\langle w'w'\rangle}^{lead}$ and a shallower mixed layer due to additional work required to maintain that layer. This shallower mixed layer could explain the reduced circulation strength $\overline{\langle w\rangle}^{lead}$ through continuity, which will be discussed in Section 4.



295



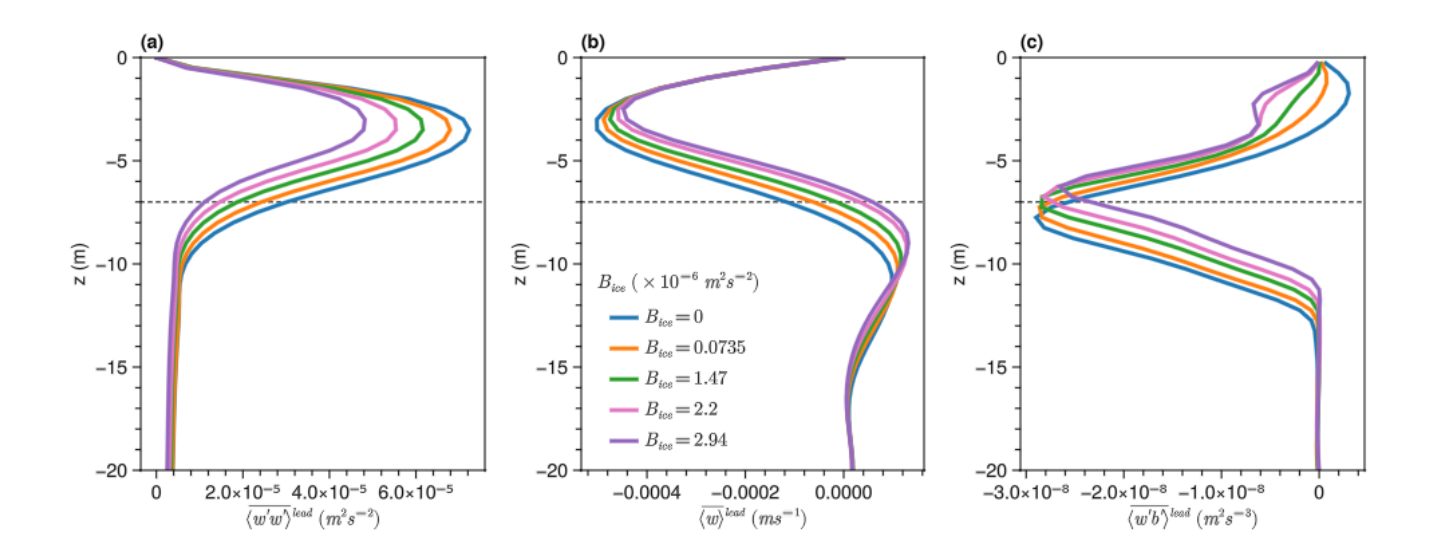


Figure 8. Sensitivity of turbulence and circulation to sub-ice freshwater flux: Same format as in Figure 7.

Changes in lead width (L_{lead}) significantly alter both the turbulence and circulation within the lead system (Figure 9). Turbulent vertical velocities $\overline{\langle w'w'\rangle}^{lead}$ are enhanced by wider leads, increasing in magnitude and depth, and reaching a plateau for $L_{lead} \geq 300$ m. In contrast, the circulation downwelling strength $\overline{\langle w\rangle}^{lead}_{min}$ is enhanced by narrower leads. This contrasting behavior of turbulence and circulation can be understood through their governing mechanisms. In these lead systems, a water parcel is primarily energized or accelerated by the surface forcing when the parcel is near the surface and within the lead, and in many cases the cross-lead circulation means that these water parcels will not be able to equilibrate with the surface forcing in the lead. As a result, narrower leads reduce the time that near-surface fluid parcels will be be energized by the surface forcing, and reduce $\overline{\langle w'w'\rangle}^{lead}$. In contrast, the circulation is primarily controlled by continuity which will be discussed in detail in Section 4. Essentially, the cross-lead circulation converges within the lead, and this converging volume of water must be downwelled by the circulation. A wider lead increases the horizontal area over which downwelling occurs in the lead, reducing the $\overline{\langle w\rangle}^{lead}_{min}$ required to export a given surface-converging water volume.

The cross-lead structure of vertical TKE (Figure 10) shows an active mixing region that is near the lead center for small leads. As the lead width increases, this active mixing region becomes more intense and moves further to the right of the wind vector. Normalizing the across-lead variations by the lead width (Figure 10b) shows that the increase in vertical TKE profiles (Figure 9a) stems from a combination of increased $\overline{\langle w'w'\rangle}^{lead}$ both at the active mixing region and across the extent of the lead region. For $L_{lead} \geq 200$ m there is also a region of vertical mixing under the ice to the right of the wind (Figure 10b between solid and dashed vertical lines), which is not affected by changes in the lead width (Figure 11).





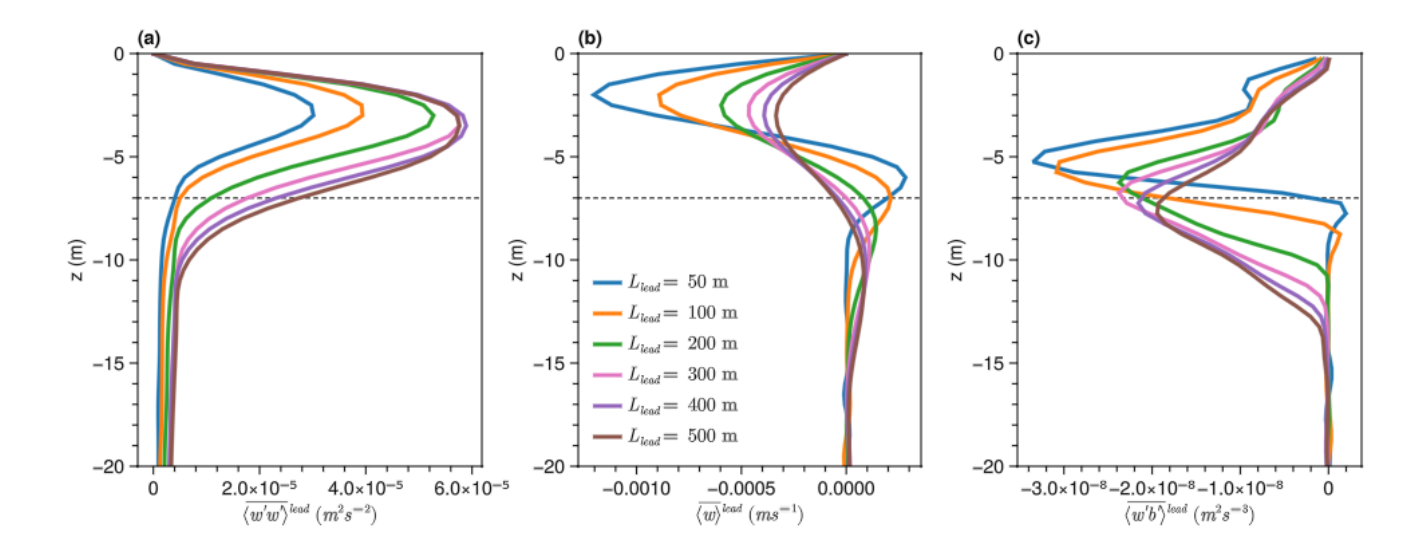


Figure 9. Sensitivity of turbulence and circulation to lead widths: Same format as in Figure 7.

The initial depth of the mixed layer depth (h_{init}) also impacts the turbulence and circulation (Fig. 12). In these experiments initial conditions use identical thermocline buoyancy profiles appended to an initially-well-mixed layer of $h_{init}=7,\,17,\,$ and 27 m depth. Deeper initial mixed layers result in more intense turbulence that penetrates further into the water column, as seen in the $\overline{\langle w'w'\rangle}^{lead}$ profiles. The initial mixed layer depth has a minor impact on the magnitude and depth of the near-surface downwelling circulation $\overline{\langle w\rangle}^{lead}_{min}$, although the deeper circulation lobe does deepen and strengthen as the initial mixed layer depth is increased.

In Figure 14, increasing f reduces turbulent intensity and weaken cross-lead circulation, as stronger rotational effects constrain vertical mixing. This reduction in mixing results from larger f enhancing inertial constraints on vertical motions, thereby suppressing Langmuir-driven overturning. With deeper h_{init} , decreasing λ not only modifies the profile shapes but produces a pronounced shift in the peak depth of $\overline{\langle w'w'\rangle}^{\text{LEAD}}$, relative to the shallower mixed-layer case shown in Figure 7. While λ has little effect on the cross-lead circulation $\overline{\langle w\rangle}^{\text{lead}}$ in shallow mixed layers, in deeper cases it substantially modifies the mean vertical velocity $\langle w\rangle$. This indicates that wavelength primarily impacts vertical mixing when the mixed layer is deep enough to interact with the Stokes depth of the surface waves, highlighting the sensitive dependence on h_{init}/δ .

These findings highlight the combined influence of wave penetration depth, buoyancy forcing, and mixed layer structure on the dynamics of turbulence in leads. A synthesis of these parameter impacts is provided in Table 2.





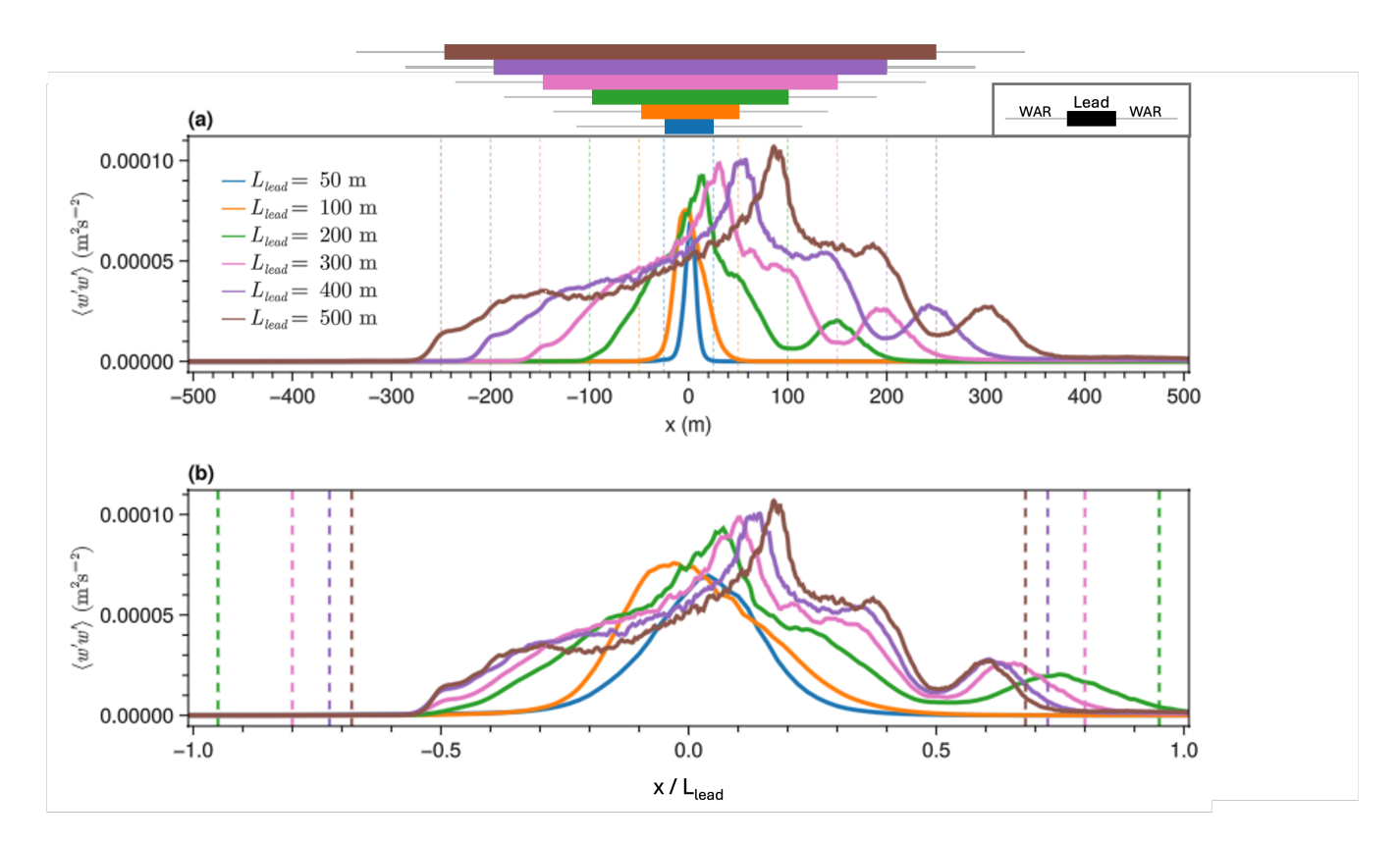


Figure 10. (a) Depth-averaged cross-section of $\overline{\langle w'w'\rangle}^{lead}$ over the top 10 m with the x-axis of the raw cross-lead distance. Overlay bars indicate the position of the lead, with colors corresponding to the legend; gray bars indicate the wave-affected regions. (b) Depth-averaged cross-section of $\overline{\langle w'w'\rangle}^{lead}$ over the top 10 m, with the x-axis representing the cross-lead distance normalized by L_{lead} . Dashed vertical lines indicate where wave-affected regions end.

315 4 Scaling the Dynamics Within Leads

4.1 Circulation Downwelling: $\overline{\langle w \rangle}^{lead}$

The surface boundary condition $\langle w(z=0)\rangle=0$ and the incompressibility of water $(\nabla\cdot\langle\mathbf{u}\rangle=\partial_y\langle v\rangle+\partial_z\langle w\rangle=0)$, means that $\overline{\langle w\rangle}_{min}^{lead}$ must be associated with cross-lead convergence of water in the layer above $\overline{\langle w\rangle}_{min}^{lead}$. Integrating the continuity equation in the vertical (z) from the depth of $\overline{\langle w\rangle}_{min}^{lead}$, which we will term $z=-D_w$ to the surface (z=0) and in the cross-lead direction





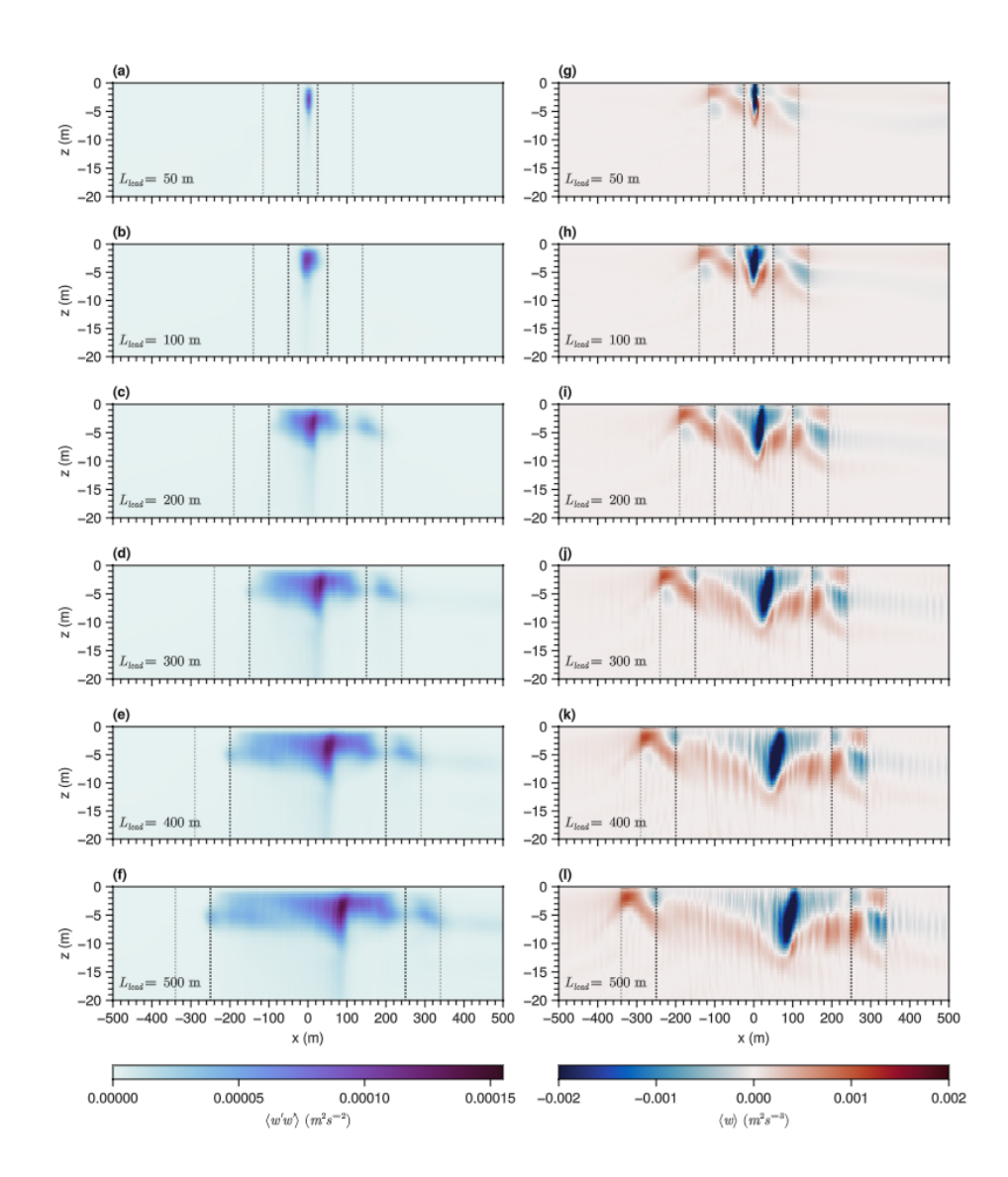


Figure 11. (a-f) Vertical turbulent velocity variance $\langle w'w' \rangle$, and (g-l) vertical turbulent buoyancy fluxes $\langle w'b' \rangle$, across lead widths ranging from 50 m to 500 m. Subpanels: (a) and (g) 50 m, (b) and (h) 100 m, (c) and (i) 200 m, (d) and (j) 300 m, (e) and (k) 400 m, (f) and (l) 500 m. Black dotted lines represent the boundaries of the lead, and gray dotted lines represent the wave-affected area.

320 from the left to right lead edges, results in the following scaling for $\overline{\langle w \rangle}_{min}^{lead}$,

$$\overline{\langle w \rangle}_{min}^{lead} \approx \int_{z=-D_w}^{0} \int_{y=-L_{lead}/2}^{L_{lead}/2} \frac{\partial v}{\partial y} dy dz$$

$$\approx \frac{D_w}{L_{lead}} \times \frac{1}{D_w} \int_{-D_w}^{0} \left(\langle v(y=-\frac{L_{lead}}{2}) - \langle v(y=\frac{L_{lead}}{2}) \rangle \right) dz.$$

$$\approx \frac{D_w}{L_{lead}} \times \overline{\langle \Delta v \rangle}^{D_w}.$$
18
(12)





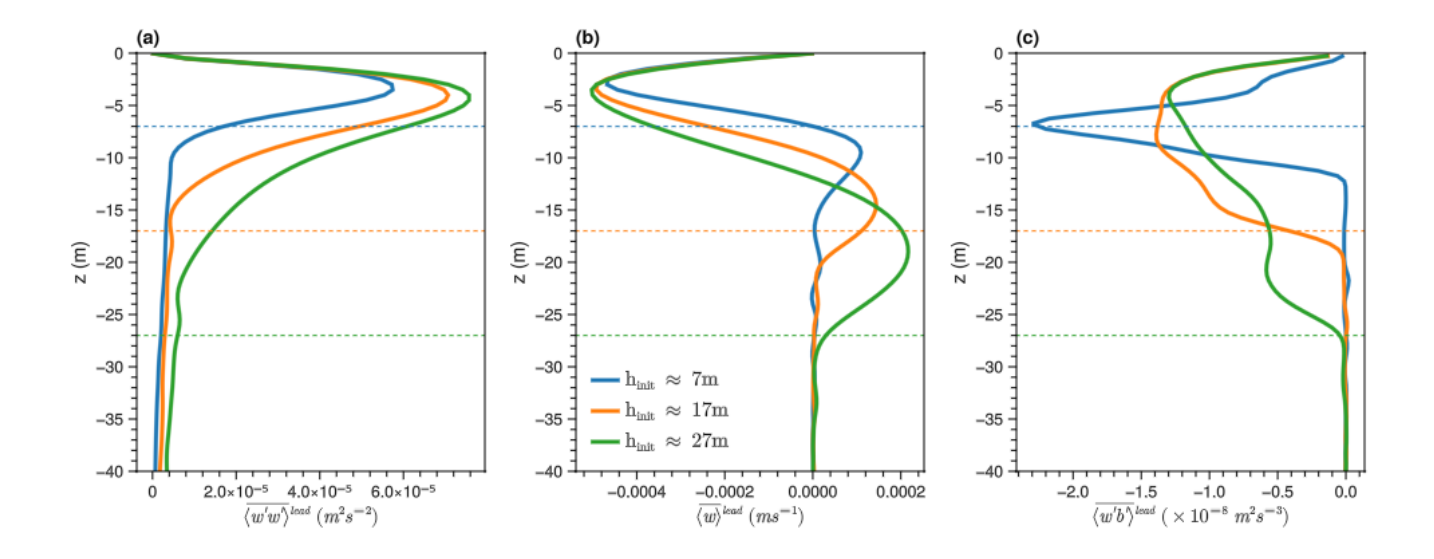


Figure 12. Sensitivity of turbulence and circulation to mixed layer depths: Same format as in Figure 7.

where $\overline{\langle \Delta v \rangle}^{D_w}$ represents the depth-averaged convergence of water within the lead in the layer between $z=-D_w$ and z=0. This scaling represents that $\overline{\langle w \rangle}_{min}^{lead}$ is controlled by two physical factors. First, $\overline{\langle w \rangle}_{min}^{lead}$ will increase if the water above is converging within the lead; i.e, the difference between the depth-integrated flow into the left of the lead and out of the right of the lead is positive which is true in the experiments here where flow at both lead edges is into the lead. Second, the converging layer's aspect ratio $\frac{D_w}{L_{lead}}$ moderates the peak downwelling. For a given vertically-averaged convergence rate, increasing the depth of the converging layer will increase the volume of convergence and accordingly will create stronger downwelling. Conversely, if the depth and strength of convergence are held constant, a wider lead will require weaker lead-averaged downwelling to maintain incompressibility, since the vertical transport of water will be over a larger horizontal area.

The aspect ratio terms in Eq. 12 can be diagnosed from the system parameters (L_{lead}) and the $\overline{\langle w \rangle}^{lead}$ profile (D_w) . The convergence of near-surface waters into the lead $(\overline{\langle \Delta v \rangle}^{D_w})$ can also be computed from the simulation data but would be more difficult to observe in practice, so it is beneficial to develop a scaling for this term. The convergence within the lead is primarily driven by local forcing within the lead, and the resulting circulation and mixing that develop. This convergent circulation constrains the time that a given water parcel can stay near the surface within the lead and be accelerated or energized by surface forcing. As such, we propose the following scaling for the near-surface convergence,

$$\frac{\overline{\langle \Delta v \rangle}^{D_w}}{u_*} = A_w f_{time} \left(\frac{\tau_{lead}}{\tau}\right) = A_w \frac{1}{1 + C_t \frac{h}{I_{tree} t}}$$
(13)





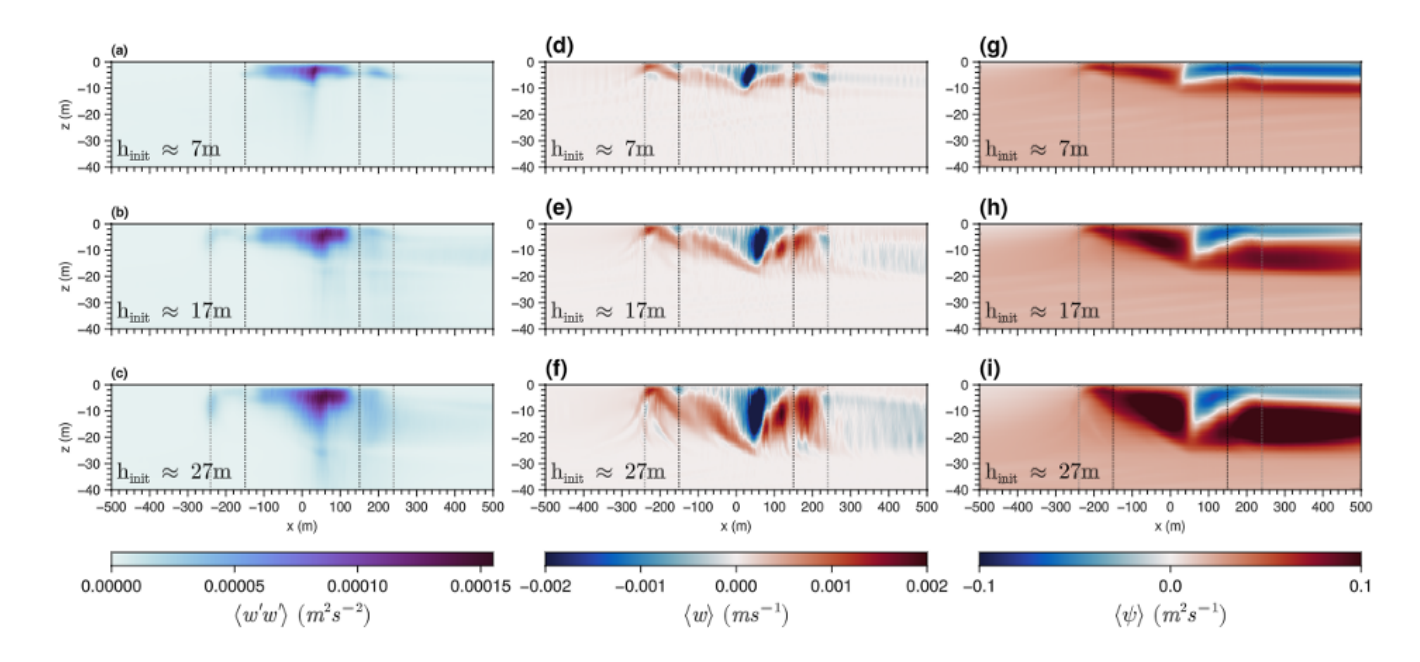


Figure 13. (a-c) Vertical velocity variance $\langle w'w' \rangle$, (d-f) vertical velocity $\langle w \rangle$, and (g-i) stream function $\langle \psi \rangle$ with different initial mixed layer depth setup. Black dotted lines represent the boundaries of the lead, and gray dotted lines represent the wave-affected area.

where A_w and C_t are constants. The function f_{time} depends on the ratio of the time that parcels spend at the surface of the 340 lead $\tau_{lead} \propto L_{lead}/u_*$ and the timescale of the dynamics $\tau \propto h/u_*$. It is designed to smoothly transition between $f_{time} = 0$ when parcels spend a very short amount of time in the lead ($\tau_{lead}/\tau \to 0$) to $f_{time} = 1$ when parcels spend many turbulent timescales within the lead ($\tau_{lead}/\tau \to \infty$) allowing their equilibration.

Substituting the convergence model (Eq. 13) into Eq. 12 provides the following model for the strength of the near-surface downwelling circulation across the lead,

345
$$\overline{\langle w \rangle}_{min}^{lead} = A_w u_* \underbrace{\frac{D_w}{L_{lead}}}_{Aspect, ratio} \times \frac{1}{1 + C_t \frac{h}{L_{lead}}}.$$
 (14)

This scaling performs well across all simulated experiments, as shown in Figure 15 using $A_w=12$, $C_t=10$ and diagnosing D_w from simulated profiles of $\overline{\langle w \rangle}^{lead}$. In the raw profiles, $\overline{\langle w \rangle}^{lead}_{min}$ varies by more than a factor of 3, whilst the scaled profiles show far less variation. In particular, the scaling captures the strengthening of downwelling for narrower leads (red symbols in Fig. 15 bottom panel), which is the primary driver of circulation changes in these simulations, and the deepening of the peak downwelling for deeper initial mixed layers. The profiles of $\overline{\langle w \rangle}^{lead}$ above the peak downwelling depth have self-similar shapes across the experiments. Equation 14 does appear to underestimate circulation strength in experiments with a small Coriolis parameter ($f=0.5\times 10^{-4}~{\rm s}^{-1}$).





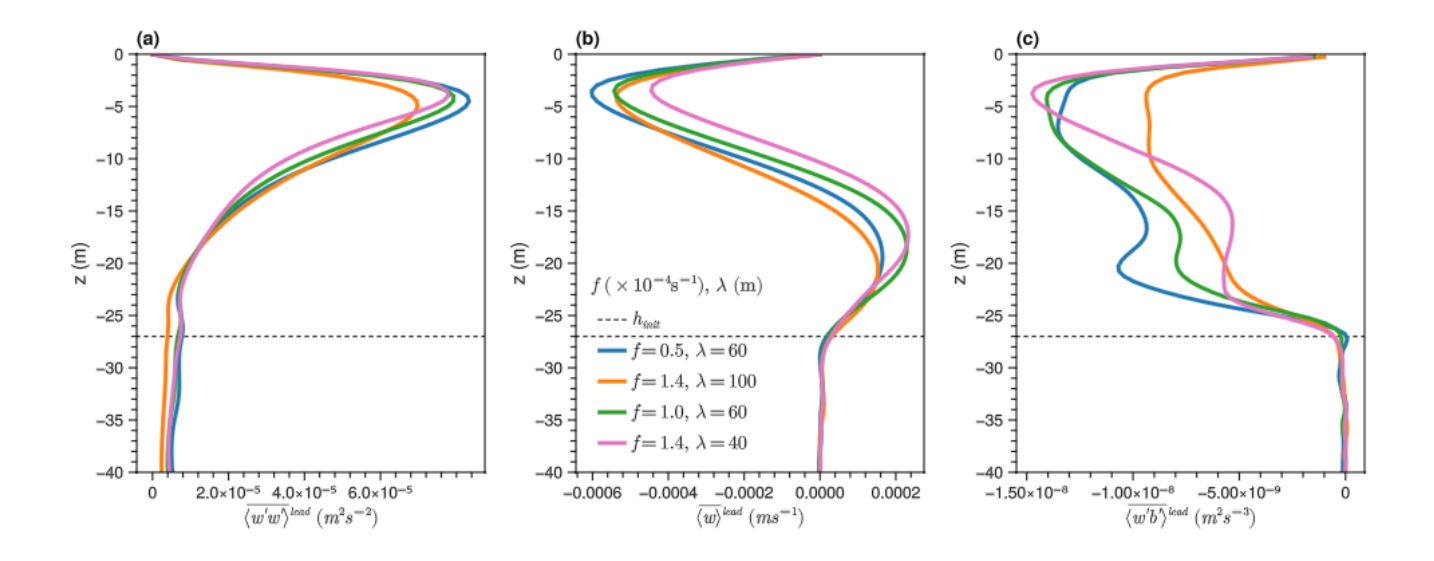


Figure 14. Sensitivity of turbulence and circulation to Coriolis parameter and wavelength with a deeper mixed layer (approx. 27 m): Same format as in Figure 14.

4.2 Turbulent Vertical Mixing: $\overline{\langle w'w' \rangle}^{lead}$

365

The wave production of $\overline{\langle w'w'\rangle}^{lead}$ per unit depth of the mixed layer can be estimated by assuming a linear profile for the along-wave Reynolds stress in the mixed layer, $\overline{\langle v'w'}^{lead}\rangle \approx -u_*^2\left(1+\frac{z}{h}\right)$, integrating the Stokes production term in Eq. 11, and dividing by the mixed layer depth h. The buoyancy term is expected to be a sink of $\langle w'w'\rangle$ in the presence of a stabilizing surface freshwater flux, and can be approximated using the energy required to mix the injected surface freshwater over the mixed layer depth (Pearson et al., 2015). Finally, the energization of water parcels by waves and surface forcing is constrained by the limited time that each parcel spends near the surface within the lead, analogous to the timescale ratio term introduced in the $\overline{\langle w \rangle}^{lead}$ scaling in equation 14.

Together, the physical models discussed above would suggest that the behavior of the lead averaged $\overline{\langle w'w'\rangle}^{lead}$ at a given depth could be captured by estimating lead-averaged terms in Eq. 11 and rearranging to find,

$$\overline{\langle w'w'\rangle}^{lead} \approx A_{ww} \left(\frac{h}{u_*}\right) \left[\frac{u_*^2 u_{s0}}{h} \left(1 - \frac{\delta}{h} \left(1 - e^{-h/\delta}\right) - C_f \frac{f\delta}{u_*}\right) - C_b B_{ice}\right] \times \frac{1}{1 + C_t \frac{h}{L_{lead}}}$$
(15)

where A_{ww} , C_f and C_b are coefficients that are to be determined, and B_{ice} is the sub-ice buoyancy flux resulting from the icemelt-driven freshwater flux. This scaling for $\langle w'w' \rangle$ includes a dependence on the surface wave length through δ . The function emulates the property that Stokes drift profiles which penetrate deeper into the water column (i.e., longer surface waves), have





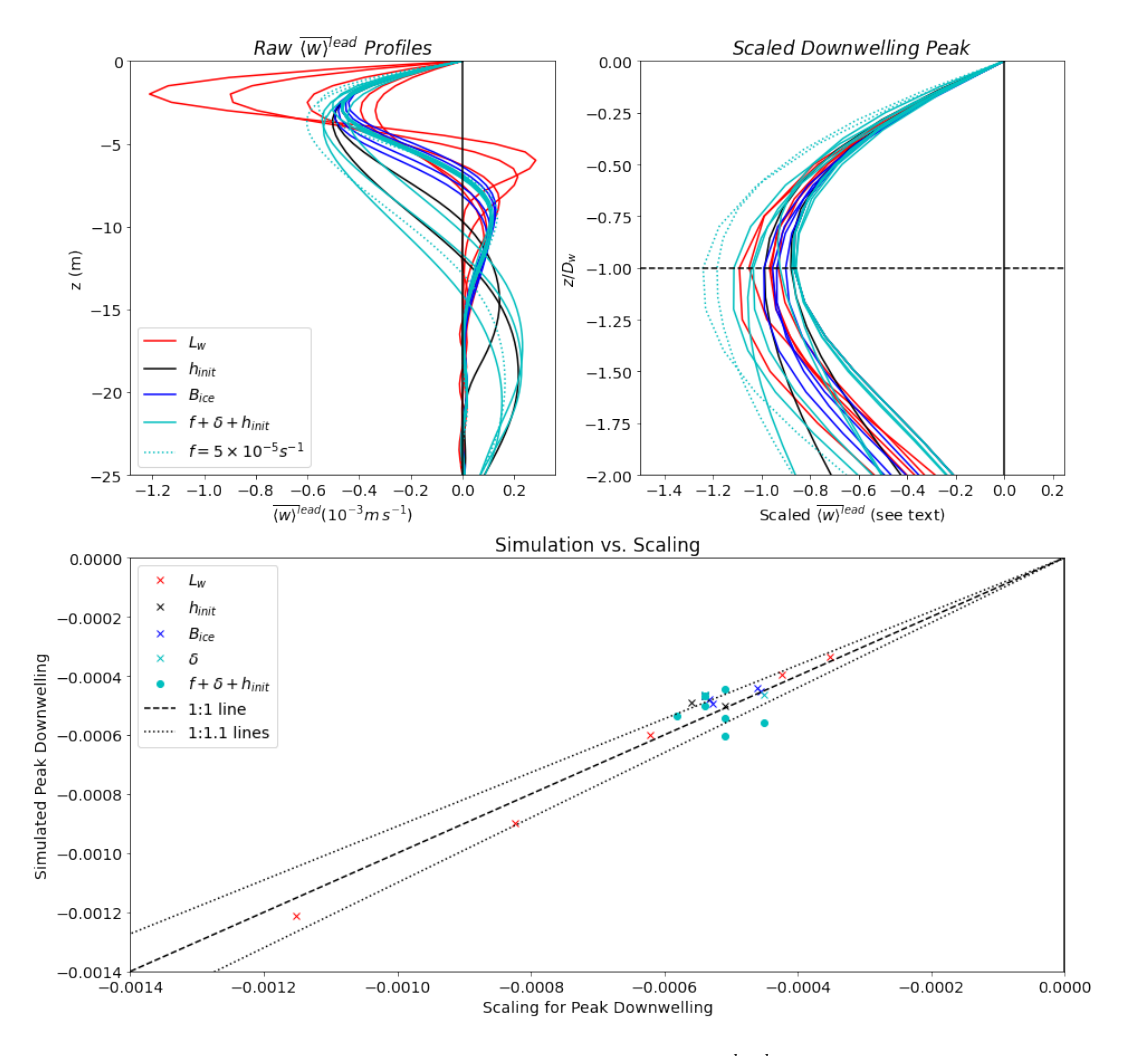


Figure 15. Test of scaling proposed in Eq. 14 for the peak circulation downwelling $\overline{\langle w \rangle}_{min}^{lead}$ using $A_w = 12$ and $C_t = 10$. The top left panel shows profiles of $\overline{\langle w \rangle}^{lead}$ for all experiments. The top right panel shows scaled profiles of $\overline{\langle w \rangle}^{lead}$ focused on the downwelling peak region. The bottom panel is a scatter plot of simulated peak downwelling vs. the scaling for peak downwelling for all experiments, along with a 1:1 line alongside 1:1.1 and 1.1:1 lines. Colors denote different sets of experiments. Dashed profiles denote experiments with small Coriolis parameter: $f = 5 \times 10^{-5} s^{-1}$.

reduced Stokes production of $\langle w'w' \rangle$ for two reasons. First, more of the Stokes drift gradient occurs deeper in the mixing layer where the Reynolds stress is weaker. Second, for very long waves or shallow mixing layers, some of the Stokes drift gradient occurs below the mixing layer and no longer contributes to $\langle w'w' \rangle$ production.

370 The C_f term in the $\overline{\langle w'w'\rangle}^{lead}$ scaling (Eq. 15) is an empirical model that accounts for the curvature of the near-surface stress $(\overline{\langle v'w'\rangle}^{lead})$ profile induced by the Coriolis effect and the presence of , and the associated reduction in Stokes production





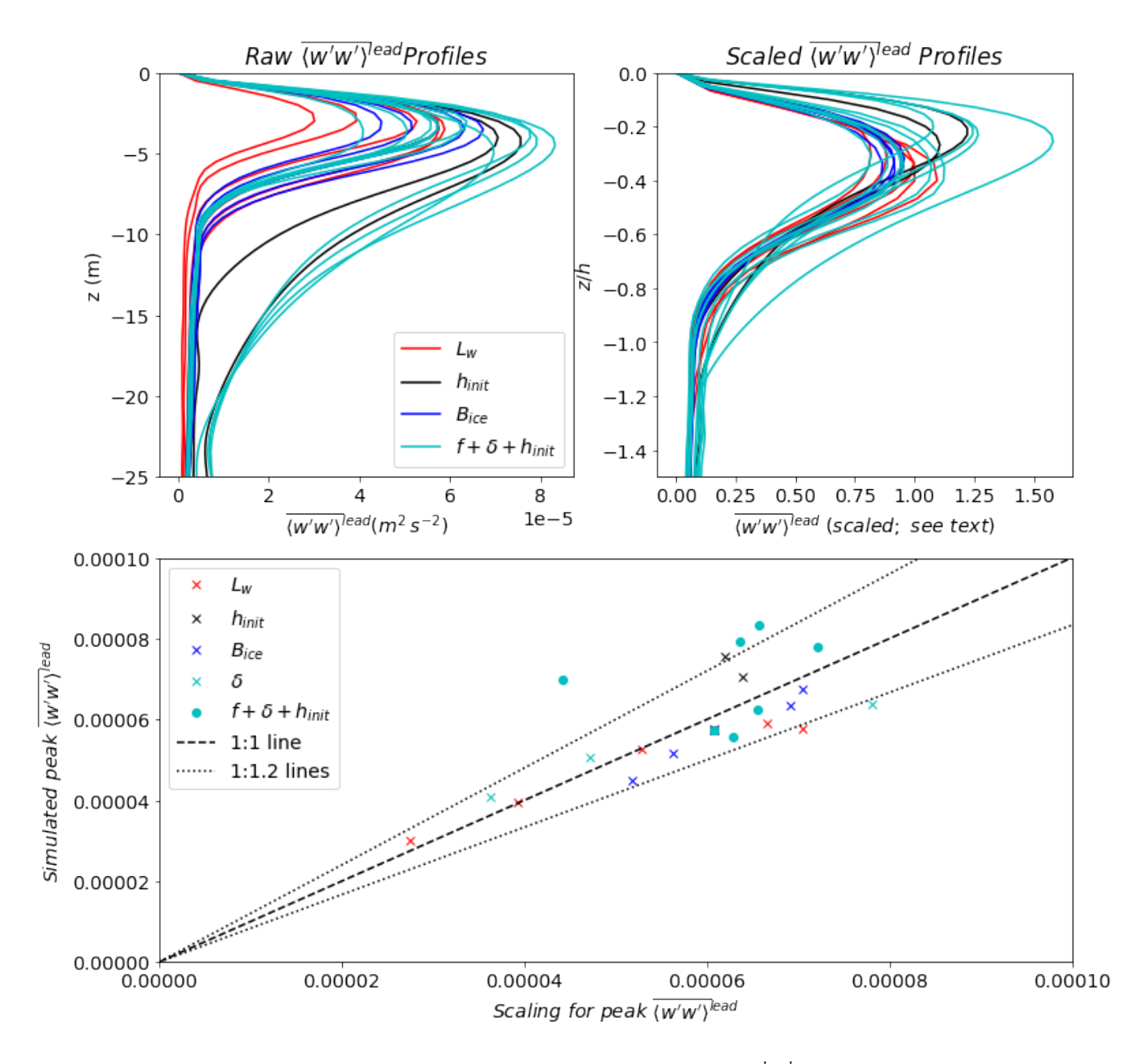


Figure 16. (a) Profiles of turbulent vertical velocity variance averaged across the lead $\overline{\langle w'w' \rangle}^{lead}$ for all simulations. (b) The same profiles as (a) but with $\overline{\langle w'w' \rangle}^{lead}$ scaled using Eq. 15 with $C_v = 0.01$, $C_t = 10$, and $A_{ww} = 3.9 \times 10^{-3}$. (c) A scatter plot showing the peak $\overline{\langle w'w' \rangle}^{lead}$ value in each simulation against the peak $\overline{\langle w'w' \rangle}^{lead}$ estimated from Eq. 15.

discussed in Grant and Belcher (2009). The C_f term is Eq. 15 is designed to reduce production most when f is large (greater curvature) or when δ is large (deeper layer of wave-induced curvature).





The scaling in Equation 15 is contrasted against the $\overline{\langle w'w'\rangle}^{lead}$ profiles and maxima in Figure 16, using $A_{ww}=0.42$, 375 $C_f=0.5, C_b=0.01$ and $C_t=10$. This scaling is able to capture the variations in peak $\overline{\langle w'w'\rangle}^{lead}$ that result from changing surface wave length (cyan crosses in Figure 16c), freshwater fluxes (blue crosses), lead width (red crosses). The simulations with deep mixed layers and strong Coriolis parameters are where the scaling performs least well, underestimating the peak $\overline{\langle w'w'\rangle}^{lead}$. Equation 15 does significantly underestimate $\overline{\langle w'w'\rangle}^{lead}$ for the simulation with the strong Coriolis force and long surface waves ($f=1.4\times 10^{-4}~{\rm s}^{-1}$ and $\lambda=100~{\rm m}$), likely suggesting a need to refine the Coriolis energy reduction term in Eq. 15 for extrema cases.

5 Conclusions

385

390

395

400

405

Sea-ice leads are dynamic environments where wind, waves, currents and turbulence interact to shape upper-ocean conditions. This study demonstrates that surface waves significantly change the circulation and turbulence beneath a simple summertime lead, and the surface conditions within the open water and under the lead-adjacent ice, which could affect the fate surrounding ice. Using a suite of simulations we found that waves intensify turbulence and mixing within the lead, particularly in a localized region near the lead center. In wave-driven simulations, near-surface vertical velocity streaks develop that are indicative of horizontal cells associated with Langmuir turbulence. These cells develop as water advects in from the lead edge, and become most intense at the downwelling region near the lead center. Waves also create a circulation on the left side of the lead (relative to the wind and wave vector), which allows a sharp front and convective mixing to develop near the lead center, and draws up deep water from to the surface under the ice to the left of the lead (Figure 3). In the presence of sub-surface heat, this upwelling could accelerate ice melt near the lead edge.

A suite of simulations was conducted with strong wave forcing to sweep the parameter space of varying lead width, surface wave length, ice melt rate, initial mixed layer depth, and Coriolis forcing. All these parameters affect turbulence, circulation, or both within the lead, and the largest changes in upper ocean dynamics are associated with variations in the lead width (varied here from 50 m to 500 m). Two novel scaling models were proposed for the strength of circulation and turbulence within the lead. These scalings show skill across the LES suite (Figures 15 & 16). The scaling for peak circulation downwelling ($\overline{\langle w \rangle}^{lead}$) was derived from the continuity equation, integrated from the surface to the downwelling peak and across the lead. The scaling for the lead-averaged turbulent vertical velocity variance peak ($\overline{\langle w'w' \rangle}^{lead}_{max}$) was based on the budget for the vertical turbulent kinetic energy averaged over the mixed layer depth. Both scalings also include a timescale multiplier that accounts for the limited time that water parcels moving across the lead spend near the surface, where they can be accelerated or energized. This timescale term tends to zero as lead width reduces, and tends to 1 for infinitely wide leads.

This work is novel in several critical aspects. First, it represents the first simulations of wave effects on upper ocean dynamics within a lead. Second, it develops physically-based models for wave-driven turbulence enhancement and circulation within the lead. These insights improve our understanding of upper-ocean dynamics in polar regions. The findings could aid parameterizations of wave-turbulence-ice interactions in global climate models, improving predictions of Arctic sea ice dynamics and future climate scenarios. This study explored wave effects in an idealized setup of stationary, melting ice and with lead-aligned





wind-wave forcing. Future work should explore more general ice-ocean wave systems, including surface-driven convection and dynamic ice.

Code and data availability. The code for the Oceananigans.jl model is freely available at https://github.com/CliMA/Oceananigans.jl (Ra-madhan et al., 2020). The extended code required to reproduce the simulations presented in this paper, along with input scripts and modeling results, can be obtained from the corresponding author. The initial temperature and salinity data used in this study were obtained from public datasets, available at https://doi.org/10.5065/D6M906SD (Stanton and Shaw, 2016).

Appendix A: Additional Boundary Conditions: Ice-Ocean Interface and Far-Field Damping

The fluxes for heat (Q_T) and salinity (Q_S) are derived from the following balance equations:

415
$$\rho_i L w_b = \rho_0 c_p Q_T - \rho_i c_i Q_i, \tag{A1}$$

$$(S_b - S_i)w_b = Q_S, (A2)$$

where ρ_i is the ice density, L is the latent heat of fusion, and $w_b = -\frac{\rho_i}{\rho_0} \partial_t h_{ice}$ is the vertical velocity of the ice-ocean interface (positive during melting). c_p and c_i are the heat capacities of seawater and ice, respectively, while Q_i is the heat flux within the ice. For summer melting conditions, $Q_i \ll Q_T$, simplifying the heat flux equation.

The parameterization of fluxes across the ice-ocean interface are based on Monin-Obukhov similarity theory formulations described in Skyllingstad and Denbo (2001) and Ramudu et al. (2018):

$$\Phi^{\text{turb}} = \frac{1}{\kappa^{\nu k}} \log \left(\frac{z_1}{z_0} \right), \tag{A3}$$

$$\Phi^{T,S} = \Phi^{\text{turb}} + 1.57 \left(\frac{u_* z_0}{\nu}\right)^{1/2} \left(\frac{\nu}{k^{T,S}}\right)^{2/3},\tag{A4}$$

where $\kappa^{\nu k}=0.4$ is the von Karman constant, $z_1=\Delta z/2$ is the vertical distance of the first computational grid point, z_0 is the basal ice roughness length, ν is molecular viscosity, and k^T and k^S are molecular thermal and salt diffusivities, respectively.

The salt flux is controlled by the melt rate, set to $\partial_t h_{ice} = 0.5 \, \mathrm{cm} \, \mathrm{day}^{-1}$, resulting in a stabilizing salt flux of approximately $1.47 \times 10^{-7} \, \mathrm{m}^2 \, \mathrm{s}^{-3}$.

A damping under ice far from the lead (i.e., in the far field of the domain) is implemented to remove waves and other transport across the periodic *x* edges of the domain. The damping strength increases gradually closer to the boundary within a width of 200 m, following a bimodal Gaussian function:

$$\eta(x) = \exp\left(-\frac{x^2}{2(200\,\mathrm{m})^2}\right) + \exp\left(-\frac{(x - L_x)^2}{2(200\,\mathrm{m})^2}\right),\tag{A5}$$

where x is the cross-lead coordinate and L_x is the total domain width in the x-direction.



450



Appendix B: Spatially-varying, along-lead Stokes drift

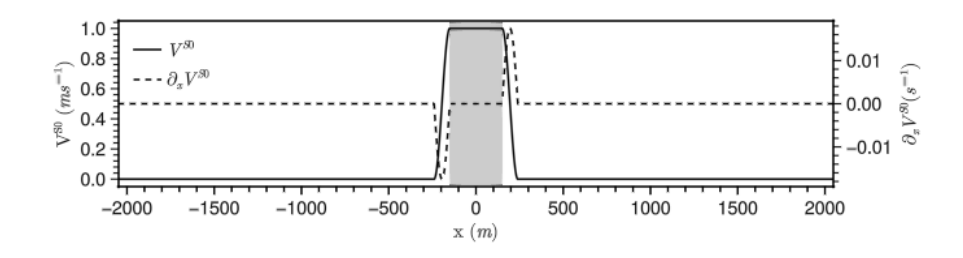


Figure B1. The surface Stokes drift V^{S0} and its horizontal gradient $\partial_x V^{S0}$. The shaded area indicates the lead.

In simulations with wave forcing, the attenuation of Stokes drift under the lead-adjacent ice is modeled using a y-dependent function:

$$\chi(x) = 0.5 \left[1 + \cos \left(\frac{\pi(x - a + \frac{b}{2})}{c} \right) \right], \quad a - \frac{b}{2} - c \le x \le a + \frac{b}{2} + c$$
(B1)

where a is the center of the lead, b is the lead width, and c is the decay width of 90 m. We term this sub-ice region where waves are still present the "Wave-affected Region" (WAR). The imposed Stokes drift, $v_s(x,z) = \chi(x)v_s(z) = \chi v_{s0}e^{z/\delta}$, decreases from its maximum value at the lead edge to zero over a distance of 90 m, ensuring that the Stokes curl is numerically well-resolved.

A validation test to explore the sensitivity of our results to the width of the Wave-Affected Region was conducted using the spatially-varying, x-oriented Stokes drift described above.

We simulated wave-affected region widths of 30 m, (10% of the lead width; Figure B2a), 90 m, (30% of the lead width; Figure B2b) and 150 m, (50% of the lead width; Figure B2c). The strength and spatial patterns of circulation within the lead, which is the focus of our analysis, are relatively unaffected by these significant changes in WAR width. The choice of WAR width does affect the strength of currents within the WAR, consistent with the changes in the horizontal gradients and their associated forcing (Figure 3). For the narrowest WAR, the vertical velocity becomes intense at the boundary of the lead and WAR, potentially indicating poorly resolved dynamics or numerical instability due to sharp lateral Stokes drift gradients and limited simulation resolution.

We selected a WAR of 90 m, corresponding to 30% of the lead width (Figure B2b). This intermediate size effectively avoids the numerical instability and sharp transitions associated with a narrower WAR, while also preventing the excessive dilution of wave impacts characteristic of a broader WAR. Consequently, the WAR of 90 m provides a balanced and realistic representation for our simulations, optimally capturing the dynamics of wave-affected regions.





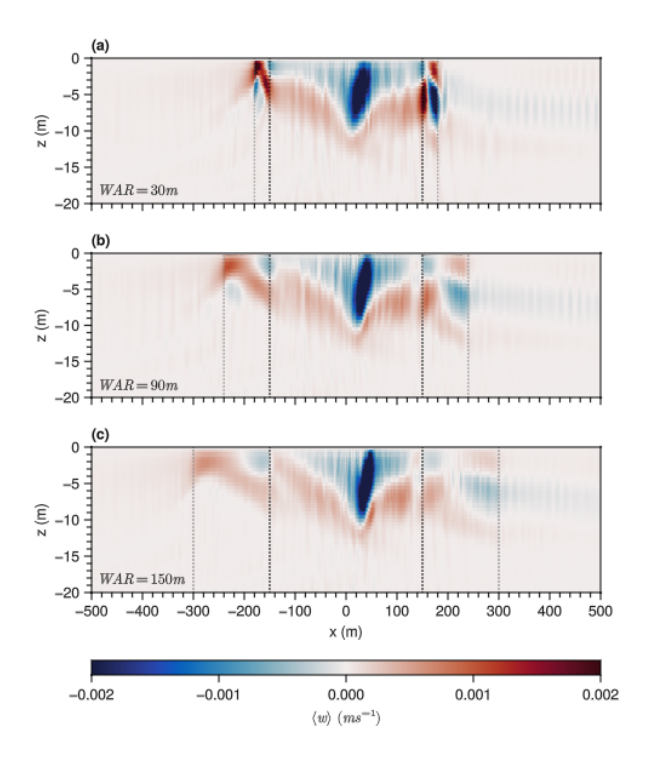


Figure B2. Vertical velocities for different WAR setups. (a) WAR = 30 m, (b) WAR = 90 m (original simulation configuration used in this study), (c) WAR = 150 m

Appendix C: Buoyancy-driven Cross-lead Circulation

455 The freshening of water at the ice-ocean interface due to ice melt, and the lack of this freshening within the lead, creates a buoyancy gradient between the lighter surface water below the ice and the denser surface water within the lead. This results in a buoyancy-driven circulation in our simulations, in addition to the wind- and wave-driven dynamics that are the focus of this paper. To demonstrate the properties and the relatively minor role of the buoyancy-driven circulation, a simulation was conducted with no wind and wave forcing and our default freshwater flux below the ice. The resulting buoyancy-driven circulation (Figure C1) is shallower and weaker than the circulation seen in wind- and wave-driven simulations (Figure 2). The buoyancy-driven circulation is confined to the upper 3 meters of the ocean within the lead and produces velocities that are an order of magnitude smaller than those in the presence of wind and waves. In contrast to the wind- and wave-driven circulation, the buoyancy-driven circulation is symmetric across the domain, with water flowing into the lead from both sides, downwelling near the lead center, and spreading out of the lead at depth.





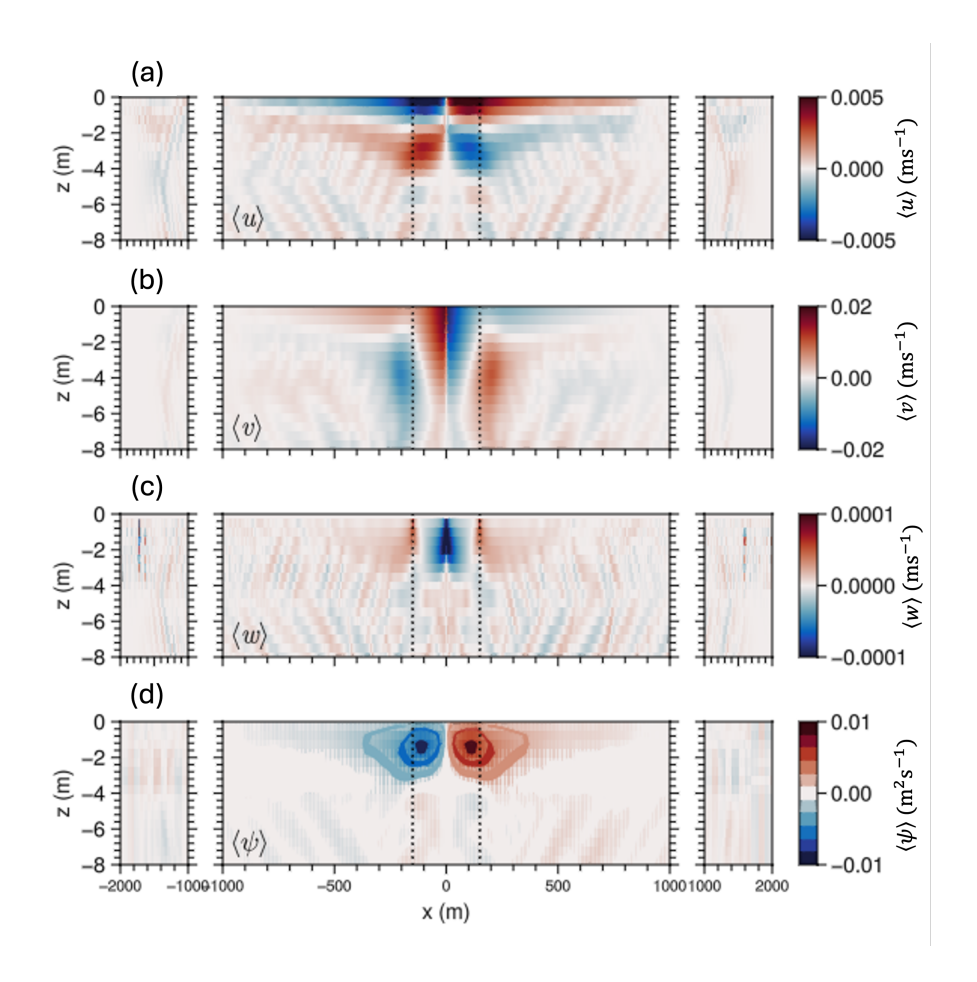


Figure C1. Cross-lead circulation under buoyancy-driven conditions. Shown are (a) along-lead velocity, (b) cross-lead velocity, (c) vertical velocity, and (d) the circulation streamfunction. Note the color axes are magnified relative to plots of wind- and wave-driven circulation in the manuscript, because the buoyancy-induced circulation is relatively weak.

465 Appendix D: Domain Size Validation

The choice of domain size is crucial to avoid artificial boundary constraints and accurately capture the physical processes being modeled. To validate this, we tested four domain configurations with the same y-sponge layer width: $(N_x, N_y, N_z) = (16384, 62, 192), (8192, 128, 192), (4096, 192, 192)$ (the original setup), and (2048, 512, 192).

As shown in Figure D1, circulation patterns remained consistent across these configurations, indicating that domain size and resolution do not significantly impact large-scale dynamics. The primary variation was in vertical velocities; increasing N_y resulted in fewer error signals in the y-averaged vertical velocities. This improvement likely stems from averaging over larger areas, smoothing out fluctuations caused by rapid temporal and spatial variations.





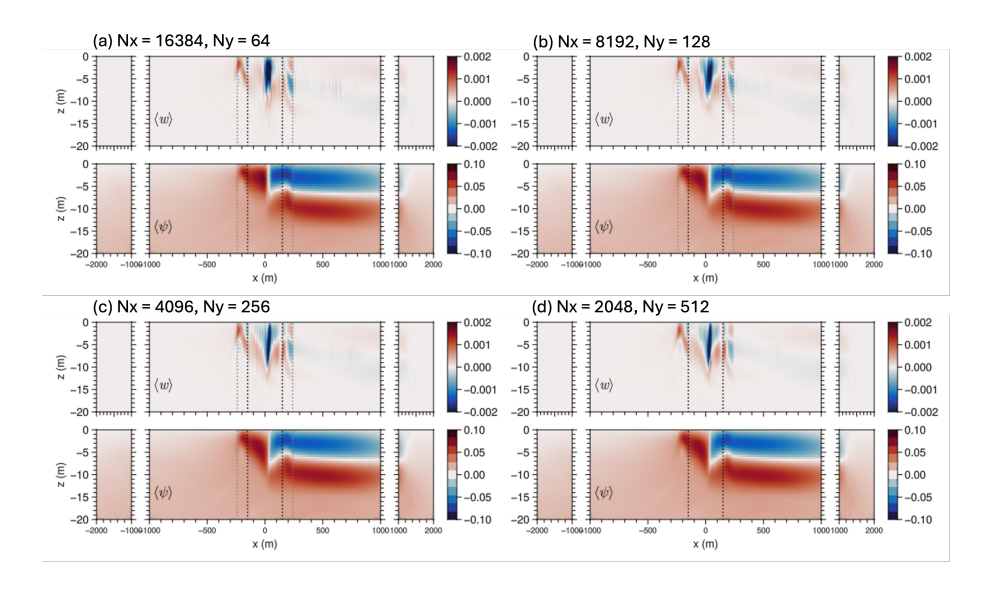


Figure D1. Stream functions and vertical velocities for different simulation setups. (a) $N_x = 16384$, $N_y = 62$, $N_z = 192$ (original simulation configuration used in this study), (b) $N_x = 8192$, $N_y = 128$, $N_z = 192$, (c) $N_x = 4096$, $N_y = 256$, $N_z = 192$, (d) $N_x = 2048$, $N_y = 512$, $N_z = 192$.

Given the consistent circulation patterns and improved vertical velocity signals with increased N_y , we conclude that the domain size (4096, 192, 192) effectively captures the essential physical processes. This configuration balances computational efficiency with optimal domain geometry, ensuring that key dynamics of Langmuir turbulence and lead interactions are well-resolved without far-field boundary effects.

Author contributions. AL: Conceptualization, data curation, formal analysis, investigation, methodology, software, visualization, writing (original draft preparation and reviewing/editing). BP: Conceptualization, formal analysis, funding acquisition, methodology, project administration, supervision, visualization, writing (original draft preparation and reviewing/editing). JH: Conceptualization, methodology, supervision, writing (reviewing/editing). AT: Visualization, writing (reviewing/editing). CH: Conceptualization, funding acquisition, methodology, writing (reviewing/editing).

Competing interests. The authors declare that they have no competing interests.

Acknowledgements. This research was supported by the National Science Foundation, Office of Polar Programs, under award OPP-2146910. Simulations were performed on high-performance computing resources provided by Oregon State University.





485 References

490

- Alvarez, A. (2022). A model for the Arctic mixed layer circulation under a summertime lead: Implications on the near-surface temperature maximum formation. *The Cryosphere Discussions*, **2022**, 1–19. Göttingen, Germany.
- Belcher, Stephen E., Alan L. M. Grant, Kirsty E. Hanley, Baylor Fox-Kemper, Luke Van Roekel, Peter P. Sullivan, William G. Large, Andy Brown, Adrian Hines, Daley Calvert, and others. *A global perspective on Langmuir turbulence in the ocean surface boundary layer*. Geophysical Research Letters, 39(18), 2012.
- Bourgault, P., Straub, D., Duquette, K., Nadeau, L.-P., and Tremblay, B. (2020). Vertical heat fluxes beneath idealized sea ice leads in large-eddy simulations: Comparison with observations from the SHEBA experiment. *Journal of Physical Oceanography*, **50**(8), 2189–2202. American Meteorological Society.
- Casas-Prat, M., and Wang, X. L. (2020). Sea ice retreat contributes to projected increases in extreme Arctic Ocean surface waves. *Geophysical Research Letters*, **47**(3), e2019GL086678.
 - Craik, A. D. D., and Leibovich, S. (1976). A rational model for Langmuir circulations. *Journal of Fluid Mechanics*, **73**(3), 401–426. Cambridge University Press.
 - Grant, A. L. M., and Belcher, S. E. (2009). Characteristics of Langmuir turbulence in the ocean mixed layer. *Journal of Physical Oceanog-raphy*, **39**(8), 1871–1887.
- Hamlington, P. E., Van Roekel, L. P., Fox-Kemper, B., Julien, K., and Chini, G. P. (2014). Langmuir–submesoscale interactions: Descriptive analysis of multiscale frontal spindown simulations. *Journal of Physical Oceanography*, **44**(9), 2249–2272.
 - Harcourt, R. R. (2013). LA second-moment closure model of Langmuir turbulence Journal of Physical Oceanography, 43(4), 673-697.
 - Leibovich, S. (1980). On wave-current interaction theories of Langmuir circulations. *Journal of Fluid Mechanics*, **99**(4), 715–724. Cambridge University Press.
- 505 Li, Q., and Fox-Kemper, B. (2020). Anisotropy of Langmuir turbulence and the Langmuir-enhanced mixed layer entrainment. *Physical Review Fluids*, **5**(1), 013803. https://doi.org/10.1103/PhysRevFluids.5.013803
 - McWilliams, J. C., Sullivan, P. P., and Moeng, C.-H. (1997). Langmuir turbulence in the ocean. *Journal of Fluid Mechanics*, **334**, 1–30. Cambridge University Press.
- Meier, W. N., Petty, A., Hendricks, S., Bliss, A., Kaleschke, L., Divine, D., Farrell, S., Gerland, S., Perovich, D., Ricker, R., Tian-Kunze, X.,
 and Webster, M. (2024). Sea Ice, in: Arctic Report Card 2024, edited by: Thoman, R. L., Moon, T. A., and Druckenmiller, M. L., National Oceanic and Atmospheric Administration, available at: https://arctic.noaa.gov/report-card/report-card-2024/sea-ice-2024/.
 - Morison, J. H., and McPhee, M. (2001). Ice-ocean interaction. Available at: http://mcpheeresearch.com/publications/Morison&McPhee_EnOS2001.pdf.
- Pearson, B. (2018). Turbulence-induced anti-Stokes flow and the resulting limitations of large-eddy simulation. *Journal of Physical Oceanog-*515 *raphy*, **48**(1), 117–122. American Meteorological Society.
 - Pearson, B. C., Grant, A. L. M., Polton, J. A., and Belcher, S. E. (2015). Langmuir turbulence and surface heating in the ocean surface boundary layer. *Journal of Physical Oceanography*, **45**(12), 2897–2911. American Meteorological Society.
 - Pearson, B. C., Grant, A. L. M., and Polton, J. A. (2019). Pressure–strain terms in Langmuir turbulence. *Journal of Fluid Mechanics*, **880**, 5–31. Cambridge University Press.
- Polton, J. A., and Belcher, S. E. (2007). Langmuir turbulence and deeply penetrating jets in an unstratified mixed layer. *Journal of Geophysical Research: Oceans*, **112**(C9).





- Ramadhan, A., Wagner, G. L., Hill, C., Campin, J.-M., Churavy, V., Besard, T., Souza, A., Edelman, A., Ferrari, R., and Marshall, J. (2020). Oceananigans.jl: Fast and friendly geophysical fluid dynamics on GPUs. *Journal of Open Source Software*, **5**(53), 2018. https://doi.org/10.21105/joss.02018.
- Ramudu, E., Gelderloos, R., Yang, D., Meneveau, C., and Gnanadesikan, A. (2018). Large eddy simulation of heat entrainment under Arctic sea ice. *Journal of Geophysical Research: Oceans*, **123**(1), 287–304. Wiley Online Library.
 - Smagorinsky, J. (1958). On the numerical integration of the primitive equations of motion for baroclinic flow in a closed region. *Monthly Weather Review*, **86**(12), 457–466. American Meteorological Society.
- Skyllingstad, E. D., and Denbo, D. W. (2001). Turbulence beneath sea ice and leads: A coupled sea ice/large-eddy simulation study. *Journal* of *Geophysical Research: Oceans*, **106**(C2), 2477–2497. Wiley Online Library.
 - Skyllingstad, E. D., Paulson, C. A., and Pegau, W. S. (2005). Simulation of turbulent exchange processes in summertime leads. *Journal of Geophysical Research: Oceans*, **110**(C5). Wiley Online Library.
 - Stanton, T. P., and Shaw, W. J. (2016). SHEBA Upper Ocean CTD and Thermal Microstructure, Western Arctic Ocean. Arctic Data Center. https://doi.org/10.5065/D6M906SD.
- 535 Stopa, J. E., Ardhuin, F., and Girard-Ardhuin, F. (2016). Wave climate in the Arctic 1992–2014: Seasonality and trends. *The Cryosphere*, **10**(4), 1605–1629.
 - Sullivan, P. P., and McWilliams, J. C. (2019). Langmuir turbulence and filament frontogenesis in the oceanic surface boundary layer. *Journal of Fluid Mechanics*, **879**, 512–553.
- Suzuki, N., and Fox-Kemper, B. (2016). Understanding Stokes forces in the wave-averaged equations. *Journal of Geophysical Research:*Oceans, **121**(5), 3579–3596. Wiley Online Library.
 - Tavri, A., Horvat, C., Pearson, B., Boutin, G., Hansen, A., and Lee, A. (2025). Langmuir turbulence in the Arctic Ocean: Insights from a coupled sea ice—wave model. *EGUsphere*, **2025**, 1–26. Copernicus Publications.





Table 1. Constants used in the model.

| Constant | Symbol | Units | Value |
|---|------------------|------------------------------------|----------------------|
| Specific heat capacity of seawater | c_p | ${\rm J}{\rm K}^{-1}{\rm kg}^{-1}$ | 4217 |
| Coriolis parameter | f | s^{-1} | 1.4×10^{-4} |
| Typical salinity of sea ice | S_{i} | psu | 3 |
| von Karman constant | $\kappa^{\nu k}$ | - | 0.4 |
| Reference density of seawater | $ ho_0$ | ${\rm kg}~{\rm m}^{-3}$ | 1024 |
| Reference density of sea ice | $ ho_i$ | ${\rm kg}~{\rm m}^{-3}$ | 920 |
| Basal ice roughness length | z_0 | m | 1.2×10^{-5} |
| Latent heat of fusion | L | Jkg^{-1} | 3.34×10^5 |
| Maximum solar radiation | Q^0 | ${\rm W}~{\rm m}^{-2}$ | 400 |
| Surface heat flux | Q^h | ${\rm W}~{\rm m}^{-2}$ | 50 |
| Molecular kinematic viscosity of seawater | ν | $\rm m^2 \; s^{-1}$ | 1.84×10^{-6} |
| Molecular thermal diffusivity | k^T | $\rm m^2 \; s^{-1}$ | 1.38×10^{-7} |
| Molecular haline diffusivity | k^S | $\rm m^2 \ s^{-1}$ | 9×10^{-10} |
| Turbulent Prandtl number | Pr | - | 1.0 |

 Table 2. Qualitative summary each key parameter's impacts on circulation and turbulence.

| Parameter | Impact on Circulation | Impact on Turbulence / Mixing |
|--|--|--|
| Stokes depth (δ) / wavelength (λ) | Minor influence on circulation structure | Controls vertical extent of wave-driven tur- |
| | | bulence; deeper δ (longer λ) enhances near- |
| | | surface mixing and penetration into the mixed |
| | | layer |
| Ice-melt buoyancy flux $(B_{\rm ice})$ | Strengthens vertical overturning within the lead | Downward buoyancy flux erodes stratification |
| | | and deepens the mixed layer |
| Lead width (L_{lead}) | Controls size and position of cross-lead circu- | Increases vertical velocity variance and broad- |
| | lation cells; wider leads shift circulation away | ens active mixing region, with secondary mix- |
| | from center | ing under ice for $L_{\rm lead} \geq 200~{\rm m}$ |
| Initial mixed layer depth (h_{init}) | Has limited effect on near-surface downwelling | Deeper h_{init} allows turbulence to penetrate fur- |
| | strength, but deepens circulation lobes | ther into the water column |





Table 3. Summary of simulation experiments. *Values explored* indicate parameter variations; remaining parameters fixed at base values.

| Parameter | Base value | Values explored | |
|--|---------------------------------------|--|--|
| Langmuir number (La_t) | 0.3 | $0.5,0.7,\infty$ | |
| Wavelength (λ) | 60 m | 40, 80, 100 m | |
| Ice melt buoyancy flux $(B_{\rm ice})$ | $1.47\times 10^{-6}~{\rm m^2~s^{-3}}$ | $0, 0.0735 \times 10^{-6}, 2.2 \times 10^{-6}, 2.94 \times 10^{-6}$ | |
| Lead width (L_{lead}) | 300 m | 50, 100, 200, 400, 500 m | |
| Initial mixed layer depth (h_{init}) | 7 m | 17, 27 m | |
| Coriolis parameter (f) | $1.4 \times 10^{-4} \text{ s}^{-1}$ | $0.5, 1.0, 1.4 \times 10^{-4} \text{ s}^{-1}$ (combined set: see note) | |
| Combined set (with $h_{init} = 27$ m): $(f, \lambda) = (0.5 \times 10^{-4}, 60 \text{ m}), (1.4 \times 10^{-4}, 100 \text{ m}), (1.0 \times 10^{-4}, 60 \text{ m}), (1.4 \times 10^{-4}, 40 \text{ m}).$ | | | |